PSF Determination for the OSIRIS Ground-Based Observations of Dust-Reddened Quasars

A Thesis Project Presented by

Milena Crnogorčević

Department of Physics, Middlebury College, Middlebury, Vermont 05753

PHYS0705, Spring 2017

Abstract

As a continuation of the research conducted in [1], this project utilizes data obtained using the OSIRIS IFS in conjunction with the Keck AO system. We use analytic functions to model the light distribution of a central nucleus for four different post-merger galaxies. Subtracting the quasar component from the original image allows for a study and examination of potential regions of excited gas or integrated emission from stars in the host-galaxy. Together with combining the near-infrared images of the observed sources with the existing images from the HST and SDSS, this project's goal is to probe into the structural and dynamical details of a post-merger system.

Signatures

Advisor: _____
(E. Glikman)

2nd reader: _____
(A. Goodsell)

3rd reader: _____
(F. Swenton)

Date accepted: _____

Acknowledgments

I gratefully acknowledge Professor Eilat Glikman whose expertise and support know no bounds; Jonathan Kemp, for his willingness and ability to always provide computer-related pieces of advice; as well as the Department of Physics for providing me with this research opportunity and a constant guidance throughout my four years at Middlebury College.

This project is a continuation of the previously conducted research presented in [1]. However, the paper is produced to stand on its own and can be read independently from any other previous work.

Contents

List of Figures

1 Introduction

1.1 IFS Observations

The process of observing and examining properties of post-merger galaxies has been remarkably enhanced by the development of Integral Field Spectroscopy (IFS). High spatial and spectral resolution of IFS allows for a detailed study of the kinematics and dynamics of evolving systems. This technique produces a three-dimensional image of an object, storing the spectral information for every pixel in a two-dimensional field of view, proving it superior to the classical technique of long-slit spectroscopy for these kinds of observations. In this paper, I utilize the data collected with the OH Supressing Infrared Spectrograph (OSIRIS) in combination with the Adaptive Optics (AO) system at the W.M. Keck Observatory. AO is used to correct for blurring of images due to the the Earth's turbulent atmosphere. All of the observations are conducted in the near-infrared regime (1-2.4 μm in wavelength). Detailed descriptions of the OSIRIS instrumentation can be found in [1] and [2].

1.2 The Feedback Process

When two or more massive galaxies collide, their respective supermassive black holes (SMBH) eventually merge, creating a new SMBH. Observational evidence suggests that at the center of most massive galaxies resides a SMBH ($10^6 - 10^9 M_\odot$, $M_\odot = 1.989 \times 10^{30}$ kg) [3]. In a post-merger system, under the influence of gravitational torques, the gas from the outer regions of a newly-formed galaxy falls inwards, fueling the growth of a SMBH and initiating emission from the accretion disk. Energy released from the AGN heats the surrounding gas, extinguishing the star-formation in galaxies. Details of feedback and fueling processes of black holes remain

unclear to this day.

Besides supplying energy to a SMBH and stellar bulges, massive inflows of gas and dust cause obscuration of the source in the optical region, while contributing to the strong light emission in the infrared. This evolutionary phase is often referred to as ultra-luminous infrared galaxy (ULIRG). Following this stage of galaxy evolution is a phase of dust-reddened quasar. Dust-reddened quasars are found to be the most luminous non-transient sources in the observable universe.

In a post-merger system many molecular clouds undergo a gravitational collapse triggered by shocks, resulting in high star-formation rates. Hopkins *et al.* suggest a model of galaxy evolution in which the dust-reddened quasar phase happens at approximately the same time as the highest star-formation rates [4]. This model of a post-merger galaxy evolution is illustrated in Fig. 1.1. The goal of this thesis is to examine the co-evolution hypothesis by inspecting four different systems that are likely in a post-merger phase, each containing a dust-reddened quasar.

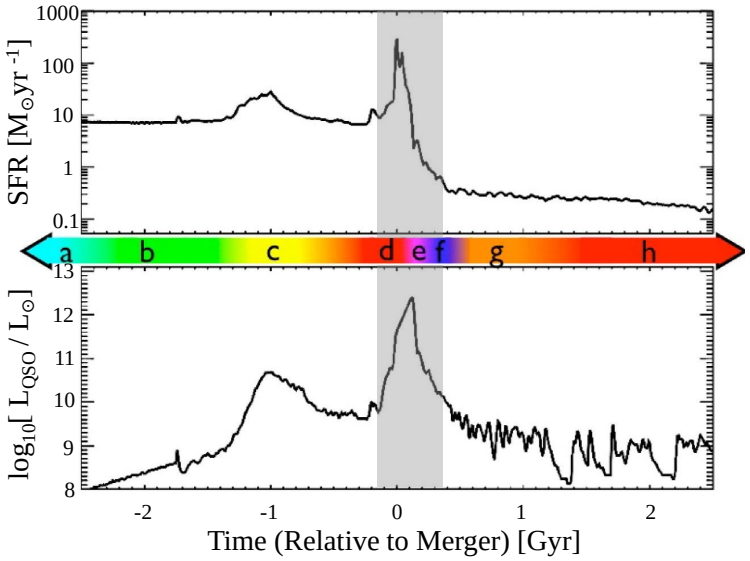

Fig. 1.1. Evolutionary stages of galaxy undergoing a gas-rich merger. Star-formation rate is presented in the upper panel, given in $M_\odot$ per a year. In the lower panel is the quasar luminosity relative to that of the Sun, L⊙. The horizontal axis represents the time relative to the merger, given in Gyrs. The peaks of both processes are shadowed in grey, corresponding to the evolutionary stage we examine in this paper. Image adapted from [1] and [4].

2 Selection, Observation, and Data Reduction

In this paper, we consider six observed targets: F2M0825+4716, F2M1507+3129, F2M1656+3821, F2M2345-1003, S82m2226-0032, and UKFS0152+0020. Their images were obtained using the OSIRIS integral-field spectrograph in conjunction with the Keck AO system on April 18, 2011; November 5, 2012; and November 6, 2012. The quasar sample was selected by matching the radio and near-infrared surveys, conducting a spectroscopic follow-up and selecting out the reddest objects [5]. The considered objects' redshifts range from $z = 0.263$ to $z = 0.988$, and their K-magnitudes span from 16.3 to 14.1. Only two objects have images from the Hubble Space Telescope (HST), shown in Fig. 2.1. Sloan Digital Sky Survey (SDSS) images of all six targets are shown in Fig. 2.2.

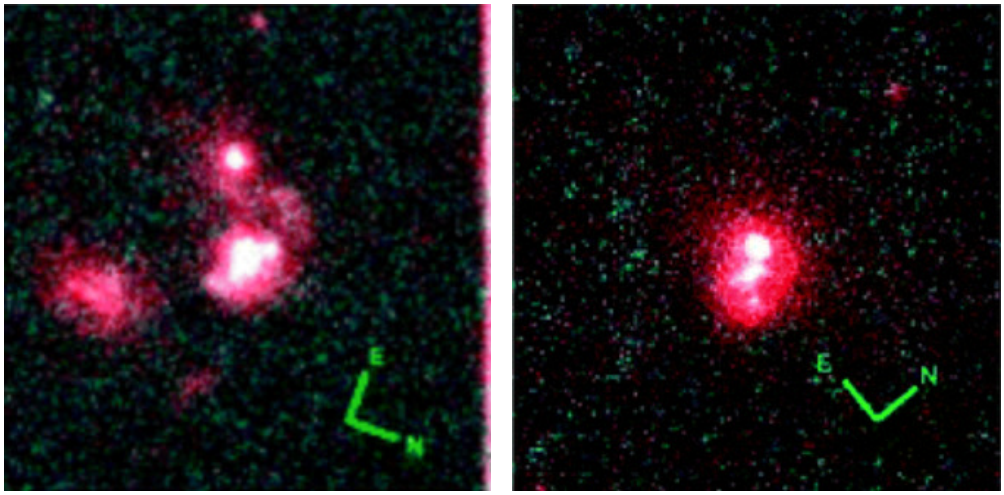

(a) F2M0825+4716 HST composite image (b) F2M1656+3821 HST composite image

Fig. 2.1. HST color composite images of (a) F2M0825+4716 and (b) F2M1656+3821. I-band data contributes to red parts, and g-band contributes to blue and green parts of the two composite images. Both systems are asymmetric and contain features that indicate potential mergers. Adapted from [6].

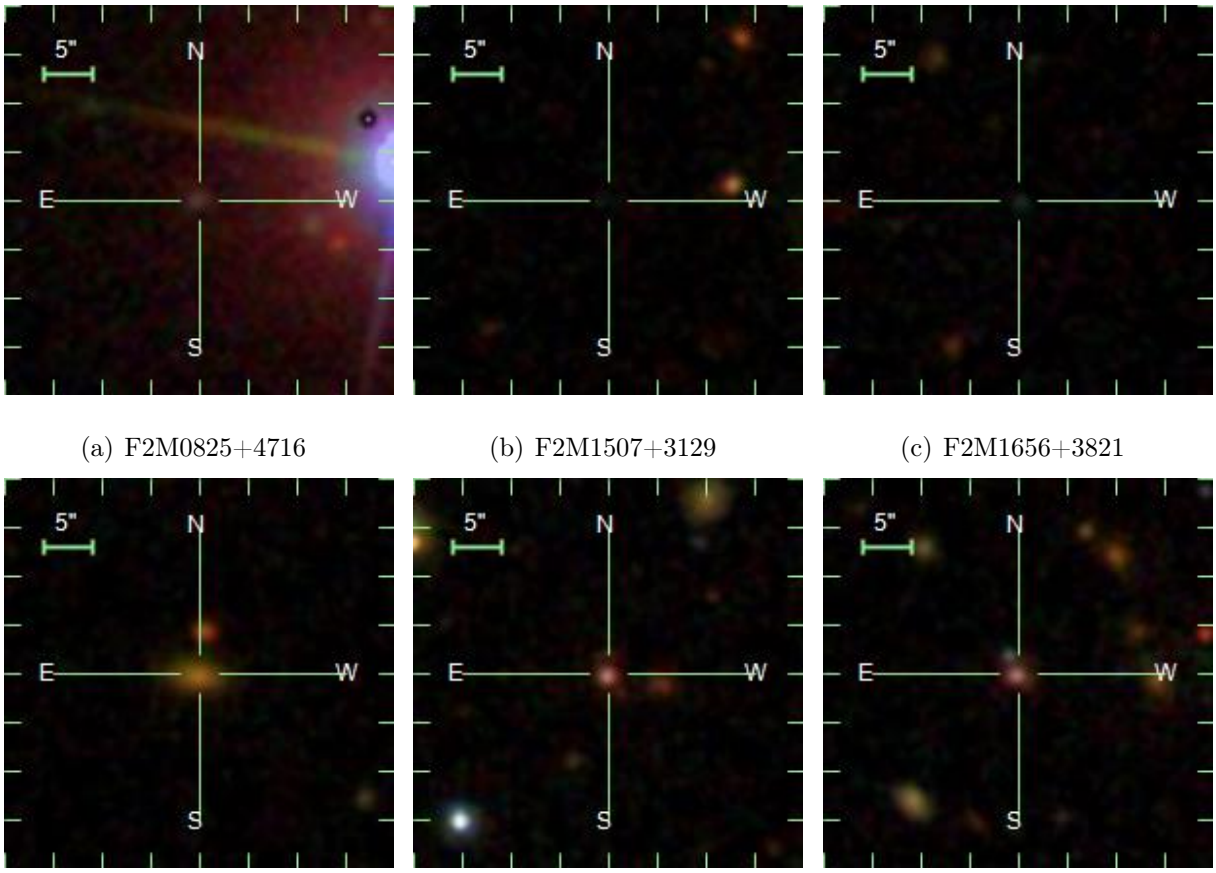

(a) F2M0825+4716 (b) F2M1507+3129 (c) F2M1656+3821

(d) F2M2345-1003 (e) S82m2226-0032 (f) UKFS0152+0020

Fig. 2.2. SDSS composites of (a) F2M0825+4716, (b) F2M1507+3129, (c) F2M1656+3821, (d) F2M2345-1003, (e) S82m2226-0032, and (f) UKFS0152+0020 combined from u-, g-, r-, i-, and z-band images. Ground-based observations from SDSS provide a significantly lower resolution as compared to those of the HST. Notice that F2M1507+3129 and F2M1656+3821 are hardly visible in SDSS due to their faintness in the optical region.

2.1 Observations and Data Reduction

Appendix A contains the observational information specific to individual objects analyzed in this paper. Step-by-step instructions for the OSIRIS data-reduction pipeline and the necessary IDL code can be found in [7] and [2]. Appendix B gives an overview of the process as applied to F2M1656+3821. Furthermore, included in Appendix C is a brief spectroscopic analysis of this source with the goal to complete the sample set study in [1].

Once the reduction process is accomplished, a three-dimensional data cube of the observed

object is produced, with two spatial dimensions and one dimension in the wavelength space. In addition to the three objects considered in [1], a set of three other objects was reduced in this project: F2M1507+3129, F2M1656+3821, and UKFS0152+0020. For F2M1507+3129 and UKFS0152+0020, data reduction process did not result in images with bright nuclei in the field of view, rendering these frames unanalyzable. Possible reason may be the faint nature of the two sources in conjunction with relatively short total integration times. Namely, F2M1507+3129 and UKFS0152+0020 are the two faintest objects in the set ($K = 15.1$ and $K = 16.3$, respectively), with the integration times of 90 min and 60 min, respectively (refer to Appendix A). A deeper observation of these two targets may be required in order to obtain meaningful frames. For reference, Appendix B contains final reduced frames of F2M1507+3129 and UKFS0152+0020 that show no concentrated light emission detected. Finally, Fig. 2.3 demonstrates slices of the successfully mosaicked data cubes for the remaining four sources, F2M0825+4716, F2M1656+3821, F2M2345-1003, and S82m2226-0032.

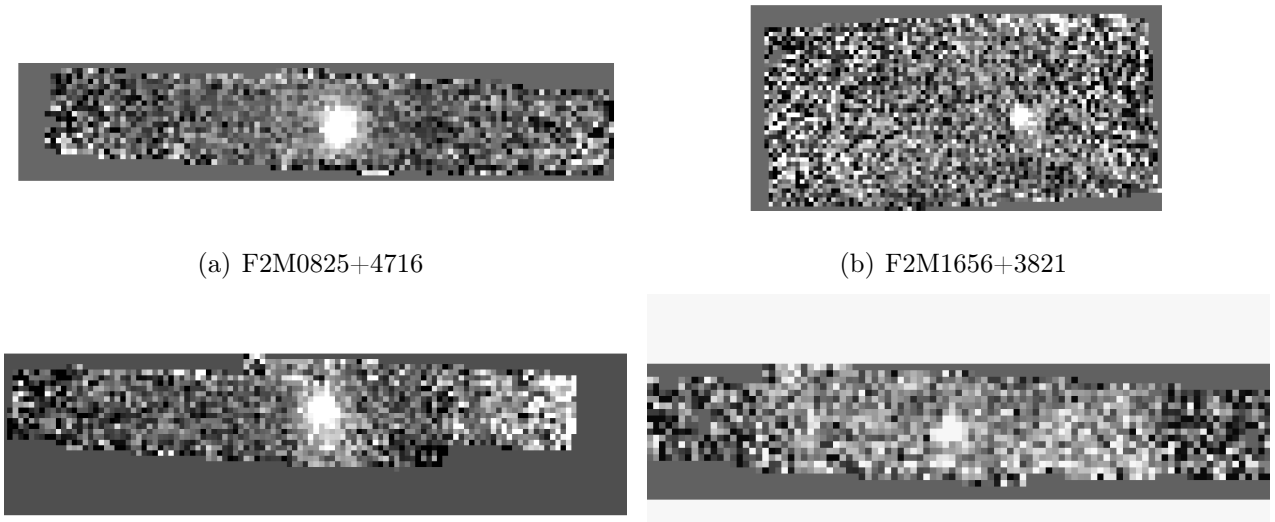

(a) F2M0825+4716

(b) F2M1656+3821

(c) F2M2345-1003

(d) S82m2226-0032

Fig. 2.3. Reduced three-dimensional data cubes, slices. Images show objects' spatial positioning in the sky. Different gradients indicate differences in intensity of the light from different regions, with white being the most intense, and black the least intense. The brightest regions represent the position of the quasar for each image, with the extended emission beyond the central nucleus coming from the host-galaxy. Each pixel in (a), (c), and (d) corresponds to an area of 0.1×0.1 arcsec^2, while a pixel in (b) is 0.05×0.05 arcsec^2.

3 Data Manipulation

Studying properties of star-formation regions in post-merger galaxies is a challenging task due to the strong light emission from an AGN that overpowers the light from the host-galaxy. To consider star-formation regions separately from the region of the central nucleus, we utilize a technique of three-dimensional modeling of surface brightness profiles of quasars. Subtracting a quasar's contribution from the original image is pivotal in our attempt to understand the host-galaxy properties that lay beneath.

AGNs are objects that are compact in size appearing as point sources [8]. However, due to their distance, atmospheric effects of the ground-based observation, and the diffraction limit of the instrumentation, they appear blurred. Figure 3.1 illustrates the extended nature of our detection for one of the sources (F2M0825+4716). To describe the observed spatial distribution of a point source—in our case a quasar—we use the Point Spread Function (PSF). Modelling a PSF for each of the sources allows for elimination of the quasar's contribution from the total light emission from the host-galaxy.

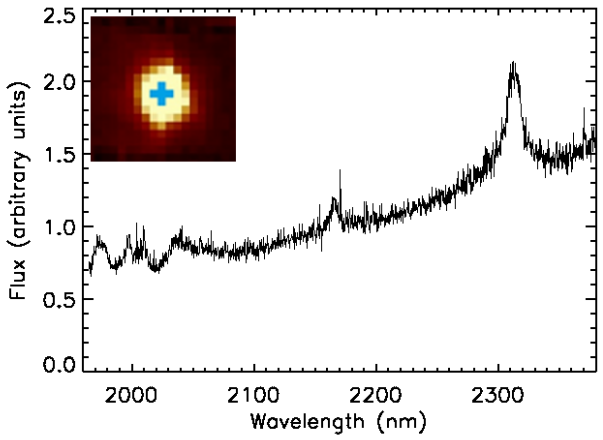

(a) Spectrum extraction area of 5 spaxel^2.

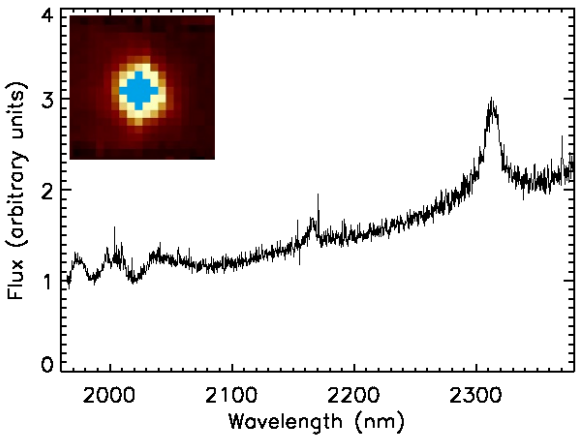

(b) Spectrum extraction area of 13 spaxel^2.

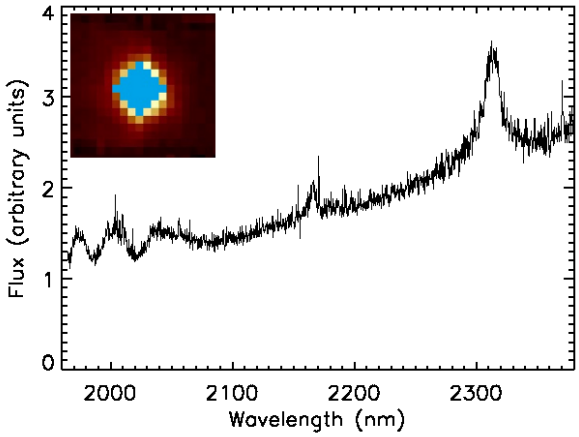

(c) Spectrum extraction area of 25 spaxel^2.

Fig. 3.1. Spectra extracted from the concentric shells of the central nucleus, F2M0825+4716. Broad emission lines, corresponding to the Paschen energy transitions of Hydrogen, Pa$_\gamma$ (rest wavelength 1094.1 nm) and Pa$_\beta$ (1282.2 nm), are characteristic feature of a quasar. They remain prominent as we increase the radius of the spectrum extraction area, though only on small scales (the extraction region's linear size in (c) is approximately 5.3 kpc [9]). This suggests that the light from the quasar overpowers the light of the host-galaxy on smaller scales. Thus, star formation on larger scales is all we can detect.

3.1 Keck Adaptive Optics System

Adaptive optics is a technique used to correct for the atmospheric turbulence and telescope aberrations, allowing ground-based telescopes to reach their diffraction limit. A detailed description of the Keck's AO system is provided in [2] and [10]. In short, the Keck AO system contains a tip-tilt mirror (TT), a deformable mirror (DM), and a beam splitter that directs the

visible light to a wave-front sensor (WFS) and the infrared light to the science camera [10]. In our observations, we use a natural guide star (NGS), a bright reference star used to measure fluctuations in the Earth's atmosphere. AO system detects distortions of the incoming wave-front and employs the DM to account for these differences in real time. This method provides a significantly improved sharpness of the image. However, as the quality of the observed image continuously changes, another piece of instrumentation—imager—is added to trace any changes in the PSF of the star. Information describing changes in the star's PSF can be used to deduce possible variations in the PSF of the science target. Characterizing the target's PSF from a ground-based observation is a relatively unexplored field of research and a problem yet to be solved.

In this paper, we determine PSFs of four quasars using analytic functions. The found PSFs are subtracted from the original galaxy images. Finally, the residual images are analyzed and overlapped with the corresponding optical images from the HST when available. If a HST image is unavailable, an SDSS counterpart is used.

3.2 PSF Determination

Using analytic functions to model the light distribution of a point source (parametric fitting) has been a widely used method to characterize the system in question [11]. In this project, we utilize radial surface brightness profiles, $\Sigma(r)$, of the Gaussian, Moffat, and Lorentzian distributions. These are analytic functions written as

$$\Sigma(r) = \Sigma_0 e^{-(r^2/2\sigma^2)} \tag{3.1}$$

for Gaussian,

$$\Sigma(r) = \frac{\Sigma_0}{\left[1 + (r/r_d)^2\right]^n} \tag{3.2}$$

for Moffat, and

$$\Sigma(r) = \frac{\Sigma_0}{1 + (r/r_d)^2} \tag{3.3}$$

for Lorentzian distribution function, where r_d is the dispersion radius, σ is standard deviation, n is the power law index, and Σ_0 is a real constant. Notice that the Moffat distribution is

reduced to the Lorentzian when $n = 1$. Using these three functions for radial profiles of a galaxy accounts for a steep decrease in luminosity with the radius, which is expected for quasars with a strong emission from the central nucleus.

3.3 σ-Clipping

Aberrant hot pixels or cosmic rays can strongly skew our efforts to fit the point source, especially when the source is faint relative to the background. To correct for this, we use σ-clipping, a commonly used technique in astronomy with the purpose of identifying and rejecting outlier pixels. Usually, these pixels are a product of the data reduction process, glitches in the instrumentation, cosmic rays, or random noise. Once the mean value, μ, of the pixels in an image is determined, one decides on the value of the σ-factor, σ_F. σ-factor is a threshold value used to identify and eliminate any pixel whose value passes beyond $\mu \pm \sigma_F \times \sigma$. The lower the σ-factor, the higher the number of eliminated pixels.

In our data set, we conduct σ-clipping for two out of four images due to their low signal-to-noise ratio, F2M2345-1003 and S82m2226-0032. To ensure that rejected pixels are not scientifically relevant to our interest, we browse through the slices in the wavelength space. Occasional presence of a bright pixel in a given location is suggestive of random error. On the other hand, the presence of a bright pixel in almost all wavelength slices suggests that there is an actual light source at the given location. A sample of the IDL code used to conduct the σ-clipping on our sources is presented in Appendix E.

4 Notes on individual objects

Spectroscopic studies of F2M0825+4716, 2M2345-1003, and S82m2226-0032 are described in detail in [1]. An equivalent analysis for F2M1656+3821 is presented in Appendix C.

In this chapter, we focus on results obtained from parametric fitting as applied to F2M0825+4716, F2M1656+3821, F2M2345-1003, and S82m2226-0032. Furthermore, we produce contour plots of the HST images shown in Chapter 2, Fig. 2.1. For the two objects with no HST images available, we produce the corresponding contour plots using the SDSS images shown in Chapter 2, Fig. 2.2. We study structural characteristics of the host-galaxy by overlaying contour plots on top of the reduced OSIRIS and residual images.

4.1 F2M0825+4716

Among the sources in our observation set, F2M0825+4716 has the longest exposure time, totaling in 210 minutes of on-course integration (Appendix A). Long exposure time provides an in-depth observation of the object, resulting in a high signal-to-noise ratio. Thus, F2M0825+4716 does not require any σ-clipping. We start our analysis by obtaining an average slice across the wavelength dimension, from $N_\lambda = 0$ to $N_\lambda = 1665$. Figure 4.1 shows (a) the averaged data cube, and (b) the flux per wavelength as a function of position of the source.

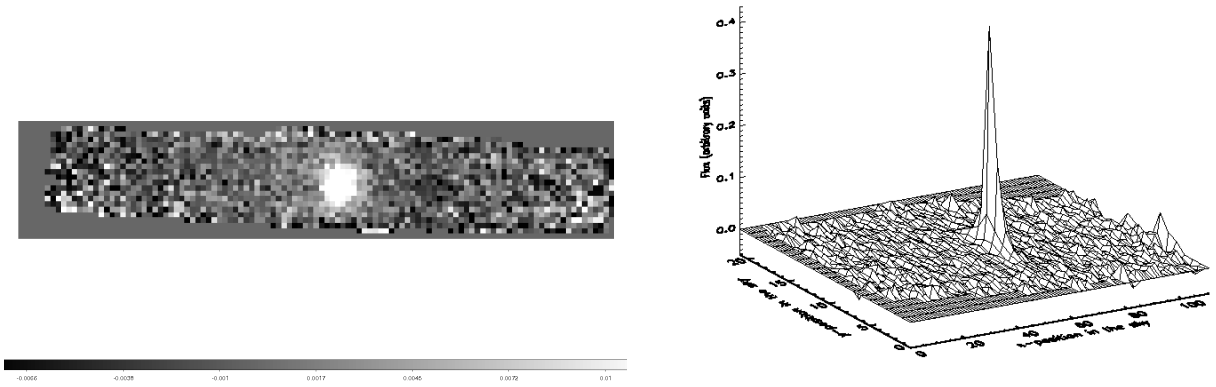

(a) Average slice of the reduced cube (b) 3D plot of the average slice

Fig. 4.1. F2M0825+4716 averaged data cube. Shown in (a) is the object's position in the sky with the color gradient indicating the relative intensity at each pixel in arbitrary units. In (b) is shown a 3D plot of the slice in (a).

Applying Eq. 3.1, we model a three-dimensional Gaussian function to fit the radial profile of the central nucleus. The resulting image and its corresponding three-dimensional plot are shown in Fig. 4.2.

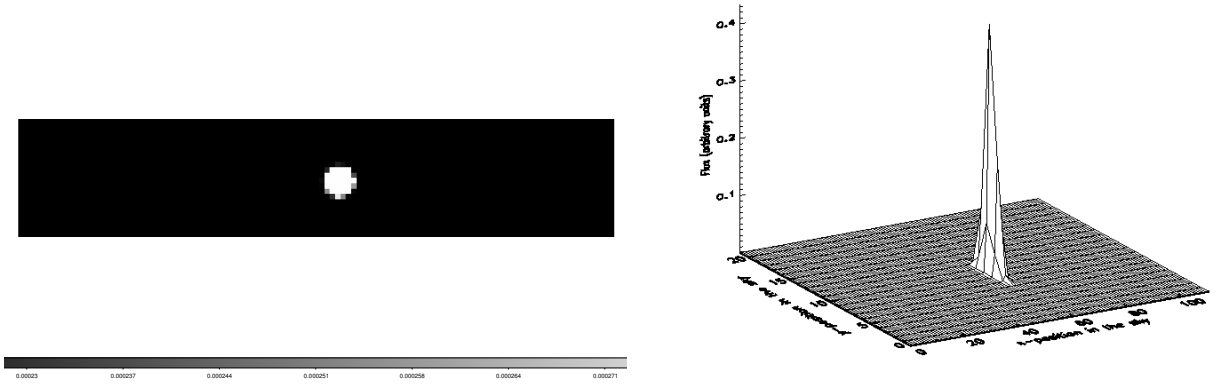

(a) Gaussian model of the average slice (b) 3D plot of the Gaussian model of the average slice

Fig. 4.2. Gaussian model for F2M0825+4716. Shown in (a) is the Gaussian radial profile of the source, and in (b) a 3D plot of the model found in (a).

Similarly, we produce the Lorentzian model for the quasar, shown in Fig. 4.3

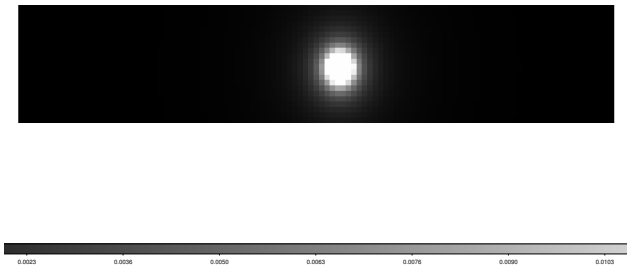

(a) Lorentzian model of the average slice

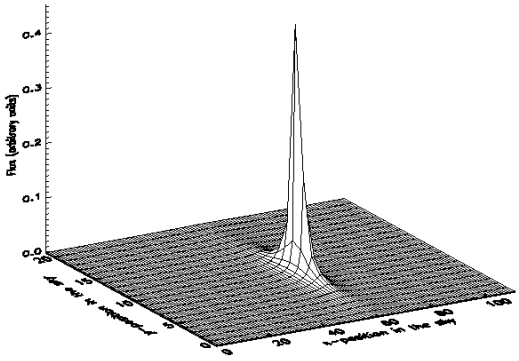

(b) 3D plot of the Lorentzian model of the average slice

Fig. 4.3. Lorentzian model for F2M0825+4716. Shown in (a) is the Lorentzian radial profile of the source, and in (b) a 3D plot of the model found in (a).

Finally, we use Eq. 3.2 to produce the Moffat model shown in Fig. 4.4.

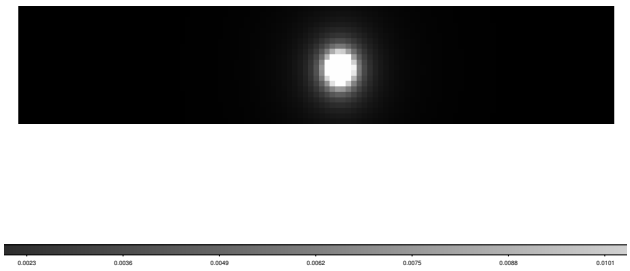

(a) Moffat model of the average slice

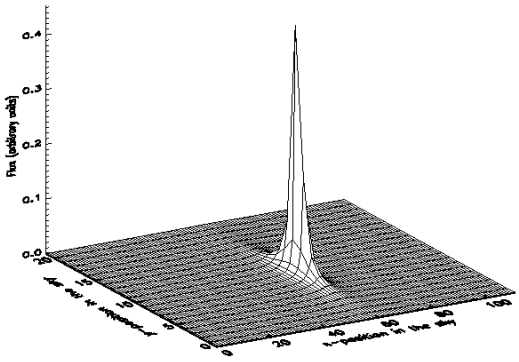

(b) 3D plot of the Moffat model of the average slice

Fig. 4.4. Moffat model for F2M0825+4716. Shown in (a) is the Moffat radial profile of the source, and in (b) a 3D plot of the model found in (a).

Notice the similarity between Fig. 4.3 and Fig. 4.4. We find that the power-law index for the Moffat function, in this case $n = 1.19410$, provides an explanation for this correspondence.

The next step in our analysis is the subtraction of models from the original image in order to

remove the quasar's contribution from the host-galaxy. Figure 4.5 shows the difference between the original image shown in Fig.4.1 and the Gaussian model shown in 4.2. We observe that, in this case, there is an over-subtraction in the central region with possible strong quasar residuals remaining intact. This is likely a poor fit.

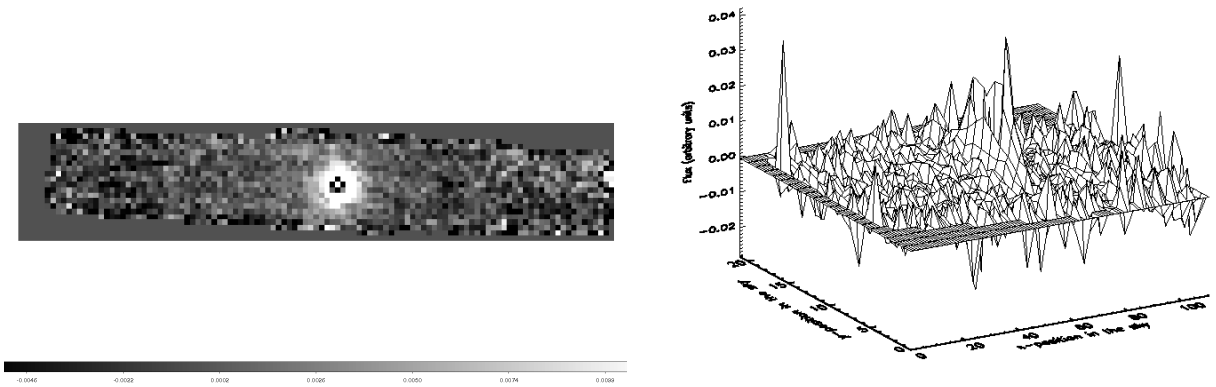

(a) Residual image after removing the Gaussian model from the original

(b) Gaussian residual, 3D plot

Fig. 4.5. Gaussian residual of F2M0825+4716. Shown in (a) is the residual image obtained by subtracting the Gaussian model from the original image and in (b) a 3D plot of (a), showing the remaining peaks in the central region, as well as over-subtractions.

Analogously, we perform the Lorentzian and Moffat subtractions, results of which are shown in Fig. 4.6 and Fig. 4.7 respectively. Here, we see a near-perfect subtraction, allowing us to study the surrounding light as free from the quasar contamination.

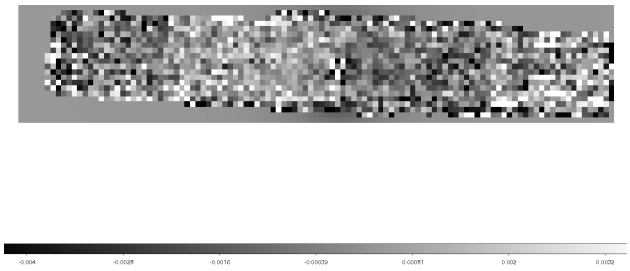

(a) Residual image after removing the Lorentzian model from the original

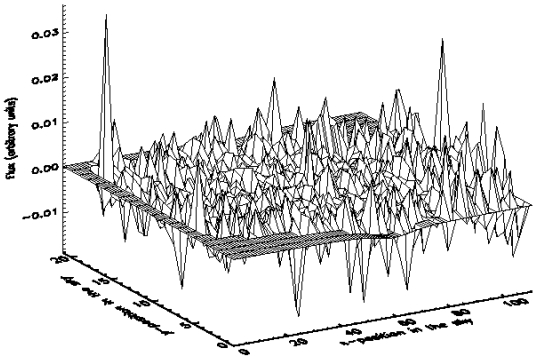

(b) Lorentzian residual, 3D plot

Fig. 4.6. Lorentzian residual of F2M0825+4716. Shown in (a) is the residual image obtained by subtracting the Lorentzian model from the original image. In (b) is shown a 3D plot of (a). Notice that the central peak is almost entirely gone.

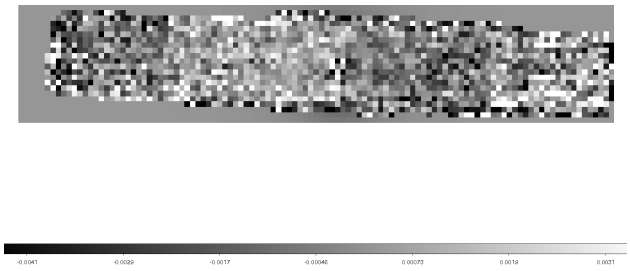

(a) Residual image after removing the Moffat model from the original

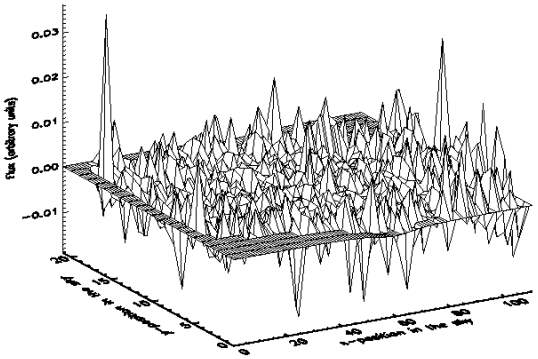

(b) Moffat residual, 3D plot

Fig. 4.7. Moffat residual for F2M0825+4716. Shown in (a) is the residual image obtained by subtracting the Moffat model from the original image. In (b) is shown a 3D plot of (a). Similarly to the Lorentzian fitting, the central peak is almost entirely gone.

By eye inspection, we conclude that the best quasar subtraction is obtained using the Lorentzian or Moffat model. Notice the bright regions surrounding the central part of the image

in Fig. 4.6(a) and Fig. 4.7(a). We suspect that these bright regions origin from the excited gas, or from the integrated emission from stars in the host-galaxy. To examine this observation, we produce a contour plot of the F2M0825+4716 HST image. We overlay the contours on top of the original average slice shown in Fig. 4.1(a) as well as the Lorentzian residual shown in Fig. 4.6. The combined images are shown in Fig. 4.8 and Fig. 4.9.

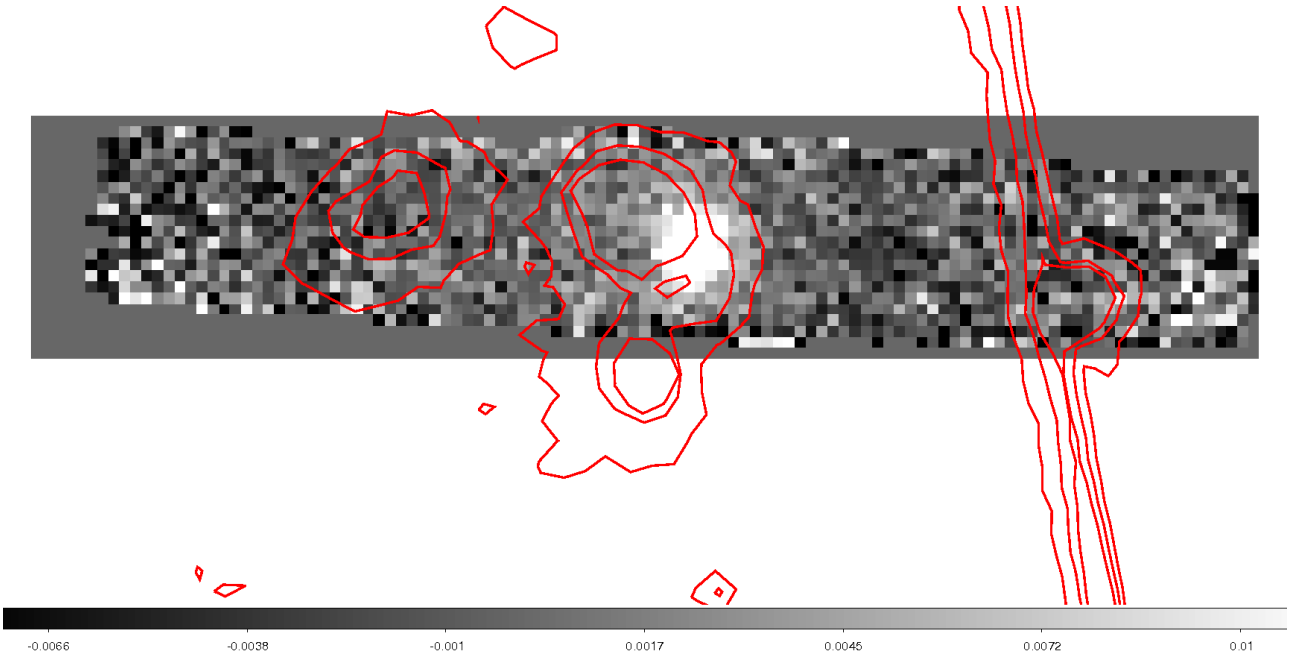

Fig. 4.8. F2M0825+4716 average slice with the corresponding HST contour plot shown in red. The central bright spot is on the edge of the contour lines, suggesting either unusual dynamics of the system, or an error in the offset.

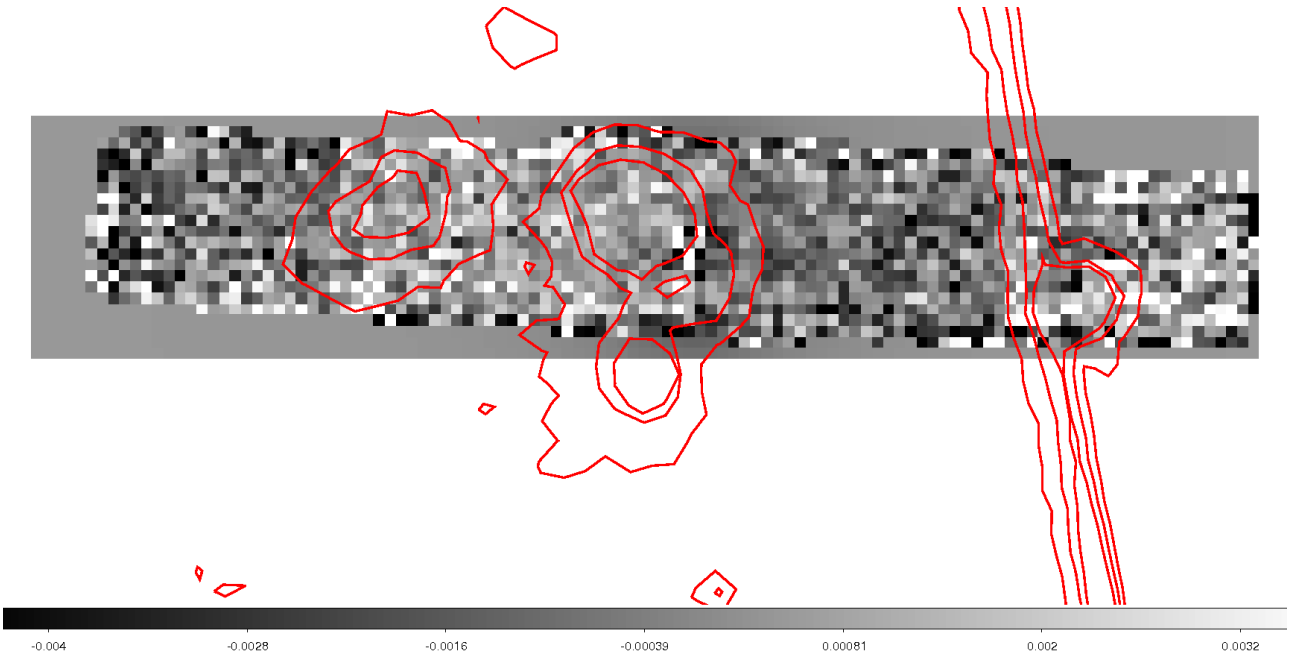

Fig. 4.9. F2M0825+4716 Lorentzian residual with the corresponding HST contour plot shown in red. Bright regions further away from the image center are now easier to detect, as the quasar emission has been subtracted. The bright regions of the image match predictions of the contour plot well.

Comparing the reduced OSIRIS image to the HST contour plot in Fig. 4.8, we observe that the quasar appears off to the side from the two contour lines that indicate a central nucleus. The same observation has been noted in [6]. We may interpret this as a recoil from a collision, suggesting a dynamic system. Another possibility might be a positional error encoded in the image headers from offsetting and tip-tilting. W.M. Keck Observatory has been contacted regarding the possible issue, but no conclusive statement can be made at this point.

4.2 F2M1656+3821

Source F2M1656+3821 has not been previously analyzed in [1]. A preview of the related observation details, as well as spectroscopic analysis can be found in Appendix C. As was the case with the previously considered object F2M0825+4716, F2M1656+3821 has a high signal-to-noise ratio, thus no σ-clipping was conducted. Analogously to the previous object, first we obtain an averaged data cube over $N_\lambda = 0$ to $N_\lambda = 449$. Figure 4.10 shows the averaged data cube in (a), and a 3D plot of flux per wavelength as a function of position in (b). Following the steps from

Sec. 4.1, we conduct an analogous parameter fitting. Figure 4.11 to Fig. 4.13 illustrate distribution functions: Gaussian, Lorentzian, and Moffat as they fit the image. Then, Fig. 4.14 to Fig. 4.16 present the corresponding residuals. For F2M1656+3821, we find the best fit to be a Gaussian. Similarly to the previous case, Lorentzian and Moffat produce almost indistinguishable results, with the power law index of $n = 1.42135$ for the Moffat distribution.

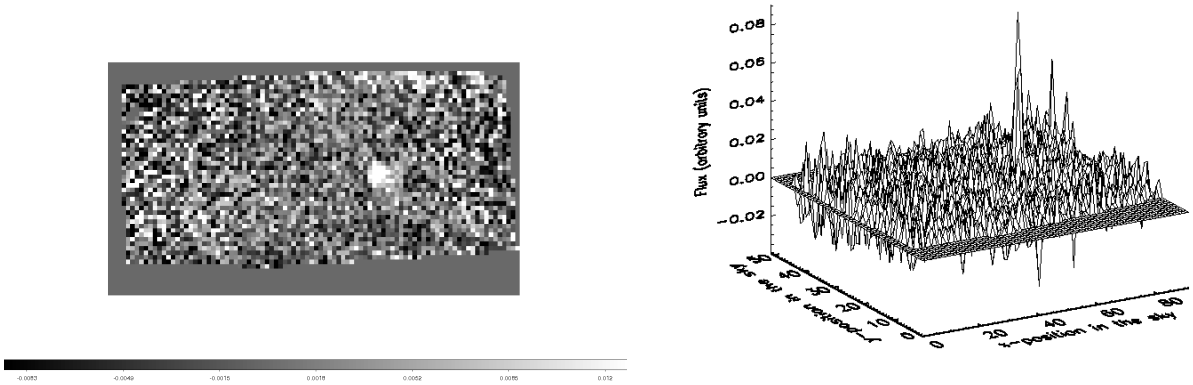

(a) Average slice of the reduced cube

(b) 3D plot of the average slice

Fig. 4.10. F2M1656+3821 averaged data cube. Shown in (a) is the object's position in the sky with the color gradient indicating the relative intensity at each pixel in arbitrary units, and in (b) a 3D plot of the slice in (a).

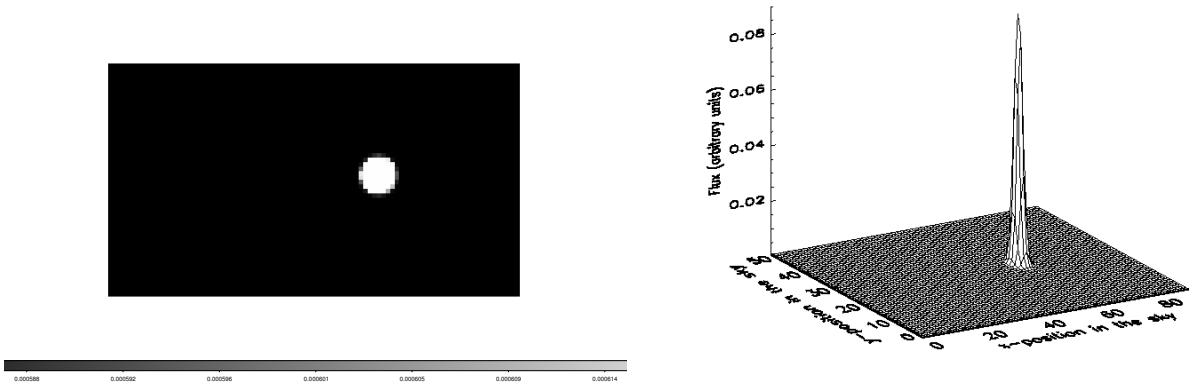

(a) Gaussian model of the average slice

(b) 3D plot of the Gaussian model of the average slice

Fig. 4.11. Gaussian model for F2M1656+3821. Shown in (a) is the Gaussian radial profile of the source, and in (b) a 3D plot of the model found in (a).

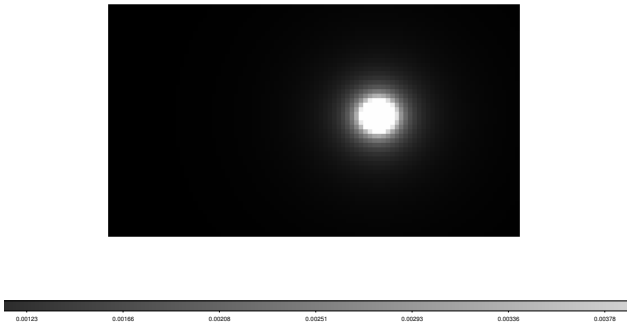

(a) Lorentzian model of the average slice

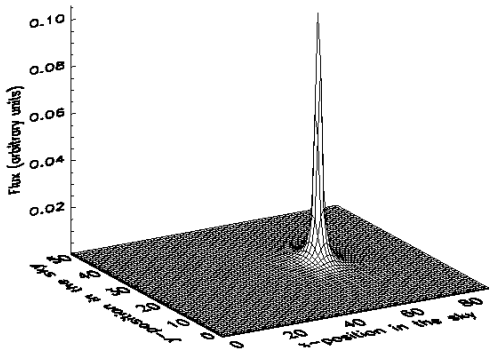

(b) 3D plot of the Lorentzian model of the average slice

Fig. 4.12. Lorentzian model for F2M1656+3821. Shown in (a) is the Lorentzian radial profile of the source, and in (b) a 3D plot of the model found in (a).

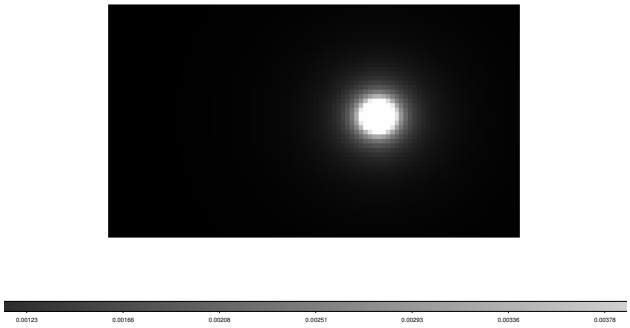

(a) Moffat model of the average slice

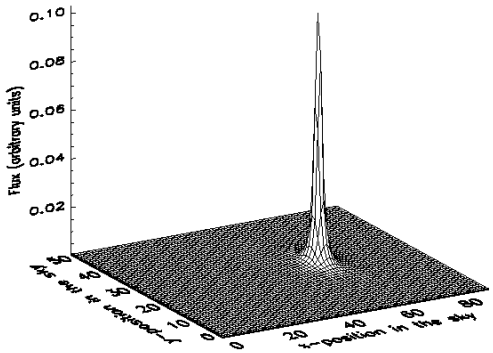

(b) 3D plot of the Moffat model od the average slice

Fig. 4.13. Moffat model for F2M1656+3821. Shown in (a) is the Moffat radial profile of the source, and in (b) a 3D plot of the model found in (a).

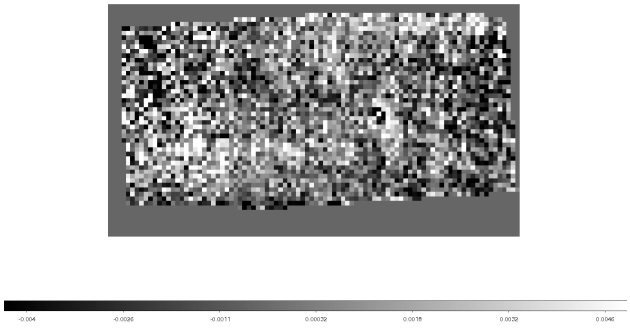

(a) Residual image after removing the Gaussian model from the original

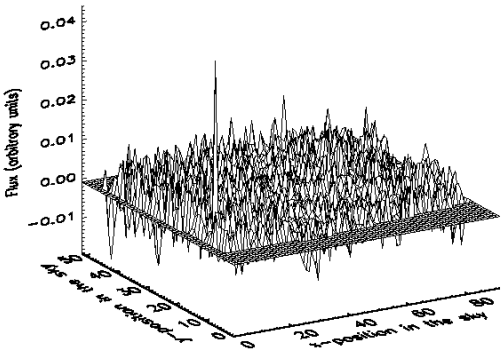

(b) Gaussian residual, 3D plot

Fig. 4.14. Gaussian residual of F2M1656+3821. Shown in (a) is the residual image obtained by subtracting the Gaussian model from the original image and in (b) a 3D plot of (a). The central nucleus has been successfully removed, with a few over-subtracted pixels in the center, and a few under-subtracted pixels in the extended region. Notice the emerged bright region in the lower left corner of (a).

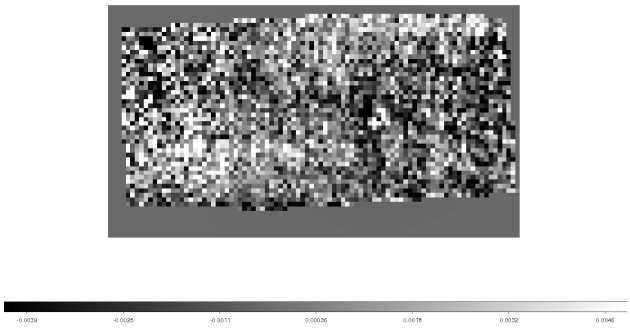

(a) Residual image after removing the Lorentzian model from the original

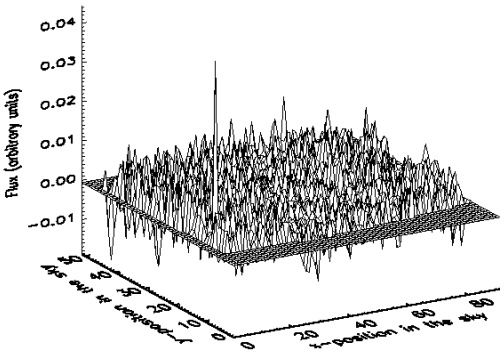

(b) Lorentzian residual, 3D plot

Fig. 4.15. Lorentzian residual of F2M1656+3821. Shown in (a) is the residual image obtained by subtracting the Lorentzian model from the original image and in (b) a 3D plot of (a). Notice the doughnut-shaped artifact resulting from an over-subtraction of the central region, and under-subtraction of the halo in its immediate surroundings.

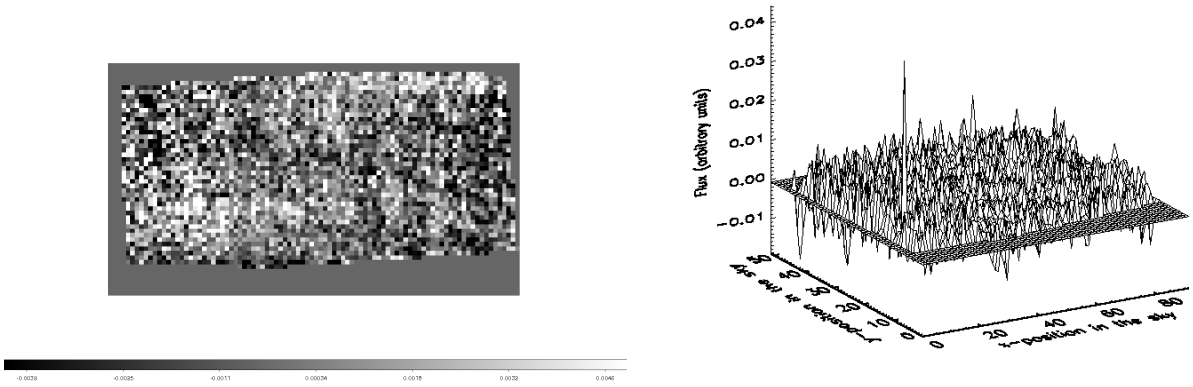

(a) Residual image after removing the Moffat model from the original

(b) Moffat residual, 3D plot

Fig. 4.16. Moffat residual of F2M1656+3821. Shown in (a) is the residual image obtained by subtracting the Moffat model from the original image and in (b) a 3D plot of (a). This result is similar to the Gaussian residual, with more bright pixels remaining in the central nucleus. Due to a power law index close to 1, this residual is similar to that of the Lorentzian model as well.

As the final step, we proceed onto fitting the HST contour plot to the original (Fig. 4.10) and the Gaussian residual (Fig. 4.14) images. Figure 4.17 and Fig. 4.18 illustrate the obtained results. Similarly to the previous target, we observe the central nucleus' slight shift relative to the contour.

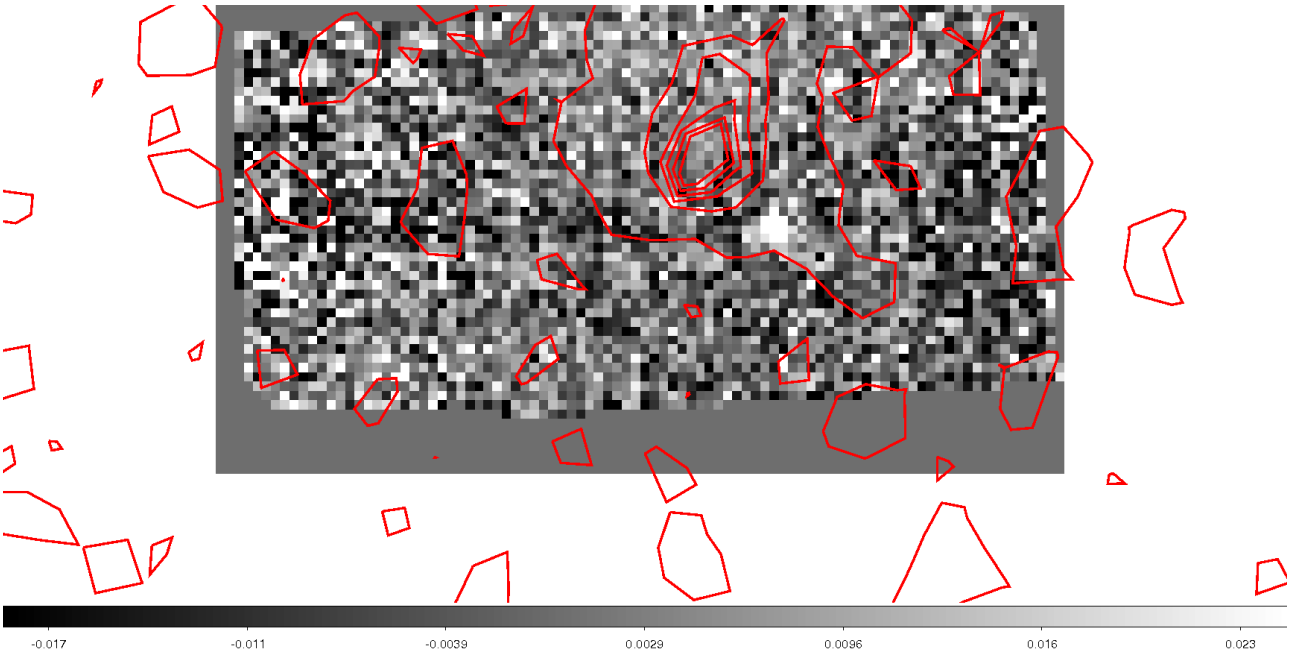

Fig. 4.17. F2M1656+3821 average slice with the corresponding HST contour plot shown in red. Similarly to the previous object, the central bright spot is on the edge of a contour line, suggesting either unusual dynamics of the system, or an error in the offset.

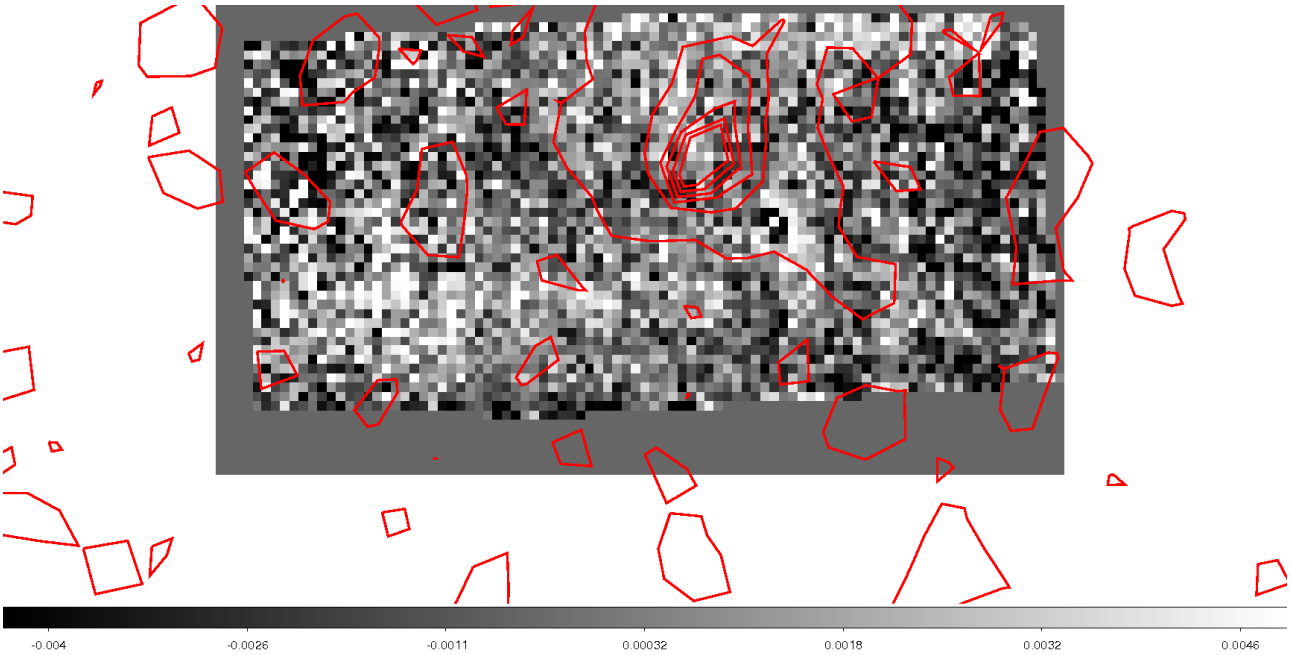

Fig. 4.18. F2M1656+3821 Gaussian residual with the corresponding HST contour plot shown in red. Notice that the bright regions in the lower left corner remain unmatched.

4.3 F2M2345-1003

F2M2345-1003 is a source observed during a total exposure time of 90 minutes of on-course integration. Some of the frames proved to contain to much noise to be used in the mosaicking process. As the result, F2345-1003 does not have a good signal-to-noise ratio, and the σ-clipping procedure was conducted with $\sigma_F = 2$. The averaged data cube is shown in Fig. 4.19, averaged over $N_\lambda = 0$ to $N_\lambda = 1651$. The 2σ-clipped image, shown in Fig. 4.20, was used for the modelling purposes. Figure **??** to Fig. 4.23 present the 3D models: Gaussian, Lorentzian, and Moffat. Figure 4.24 to Fig. 4.26 show the corresponding residual images.

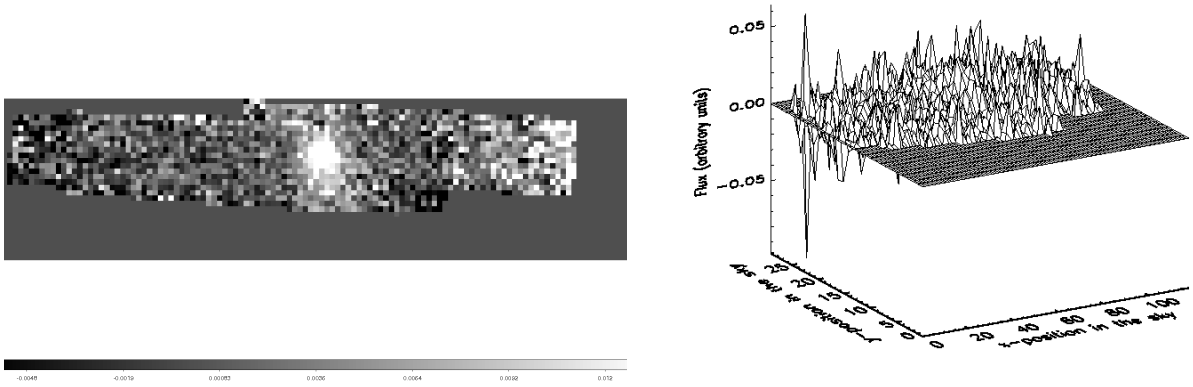

(a) Average slice of the reduced cube

(b) 3D plot of the average slice

Fig. 4.19. F2M2345-1003 averaged data cube. Shown in (a) is the object's position in the sky with the color gradient indicating the relative intensity at each pixel in arbitrary units. In (b) is shown the 3D plot of the slice in (a). Notice no prominent peak in (b).

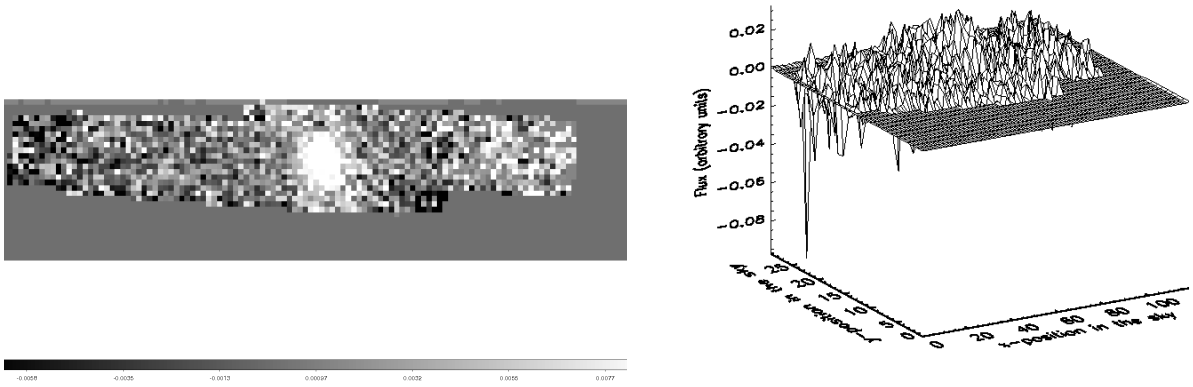

(a) 2σ-clipped average slice of the reduced cube

(b) 3D plot of the 2σ-clipped average slice

Fig. 4.20. 2σ-clipped image of F2M2345-1003. Peaks that we suspect are random noise of the image in each slice, and then averaged. This image is used for all the subsequent modeling procedures.

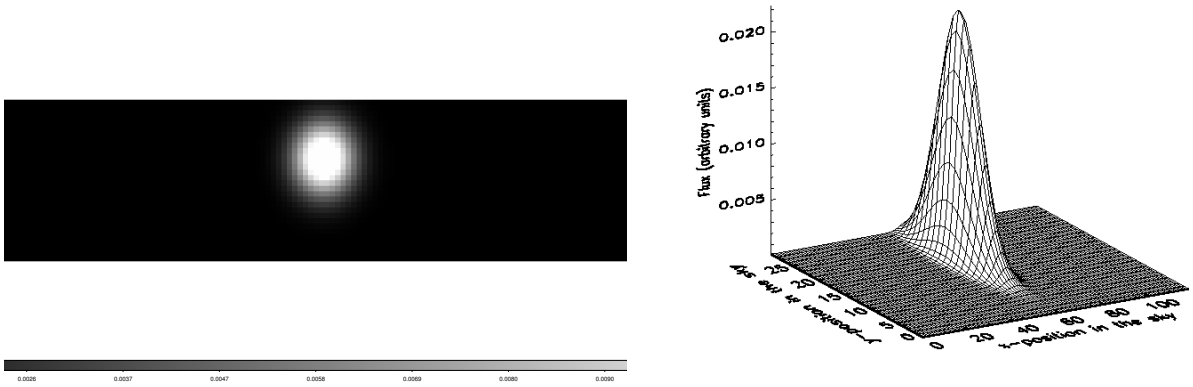

(a) Gaussian model of the 2σ-clipped average slice

(b) 3D plot of the Gaussian model of the 2σ-clipped average slice

Fig. 4.21. Gaussian model for the 2σ-clipped F2M2345-1003. Shown in (a) is the Gaussian radial profile of the source, and in (b) a 3D plot of the found model in (a).

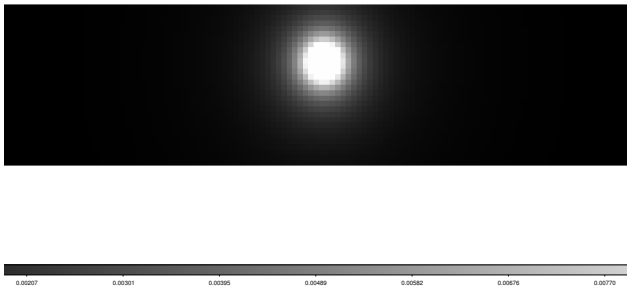

(a) Lorentzian model of the 2σ-clipped average slice

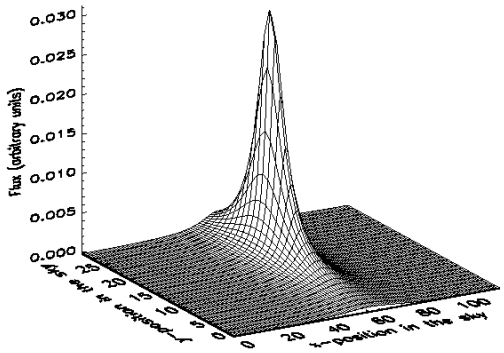

(b) 3D plot of the Lorentzian model of the 2σ-clipped average slice

Fig. 4.22. Lorentzian model for the 2σ-clipped F2M2345-1003. Shown in (a) is the Lorentzian radial profile of the source, and in (b) a 3D plot of the found model in (a).

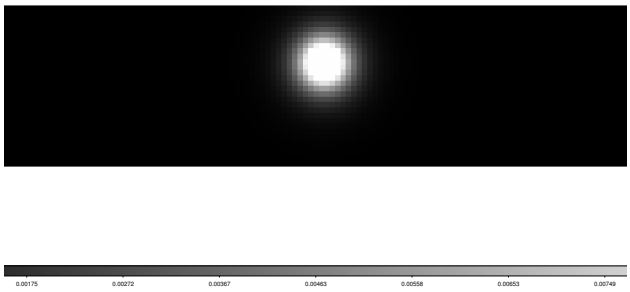

(a) Moffat model of the 2σ-clipped average slice

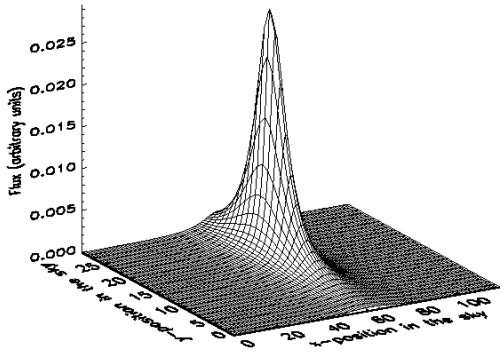

(b) 3D plot of the Lorentzian model of the 2σ-clipped average slice

Fig. 4.23. Moffat model for the 2σ-clipped F2M2345-1003. Shown in (a) is the Moffat radial profile of the source, and in (b) a 3D plot of the found model in (a).

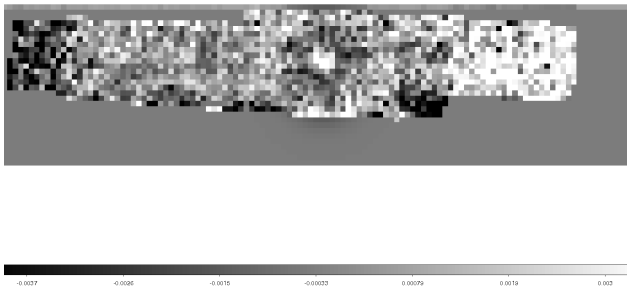

(a) Residual image after removing the Gaussian model from the original

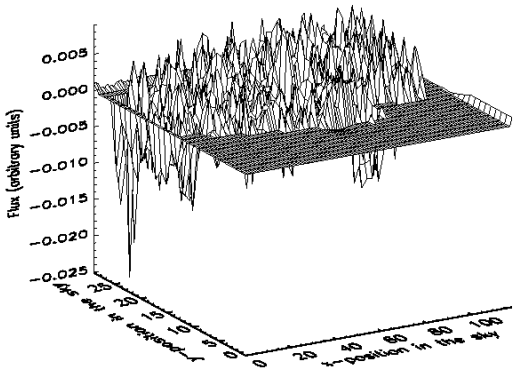

(b) Gaussian residual, 3D plot

Fig. 4.24. Gaussian residual of F2M2345-1003. Shown in (a) is the residual image obtained by subtracting the Gaussian model from the original image and in (b) a 3D plot of (a). Notice a prominent doughnut-shaped central region with the bright center and over-subtracted surroundings.

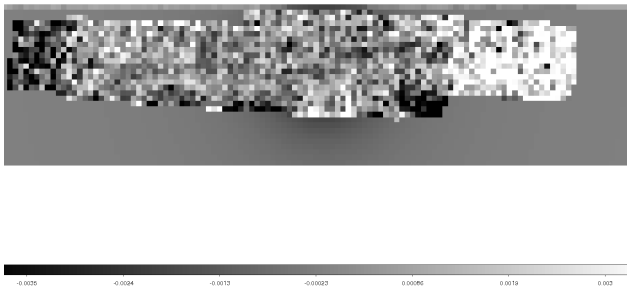

(a) Residual image after removing the Lorentzian model from the original

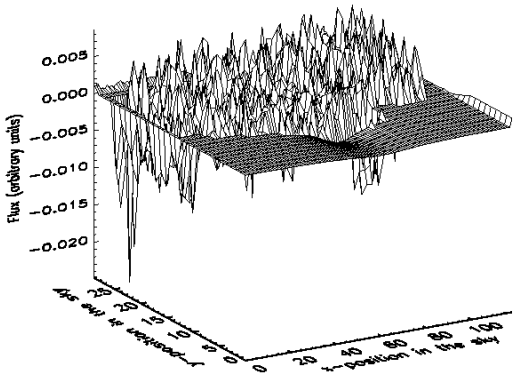

(b) Lorentzian residual, 3D plot

Fig. 4.25. Lorentzian residual of F2M2345-1003. Shown in (a) is the residual image obtained by subtracting the Lorentzian model from the original image and in (b) a 3D plot of (a). Notice a slightly less prominent doughnut-shaped artifact as the result with the bright nucleus and over-subtracted surroundings as compared to the Gaussian residual.

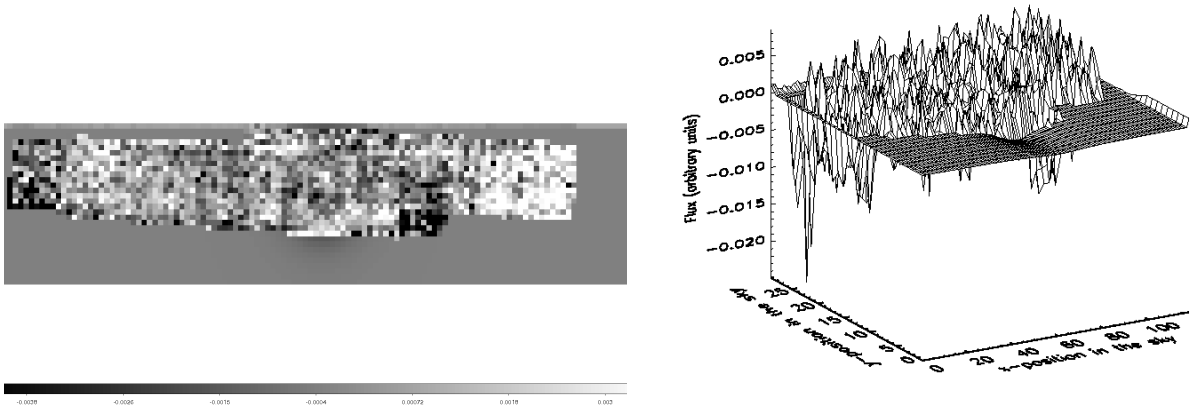

(a) Residual image after removing the Moffat model from the original

(b) Moffat residual, 3D plot

Fig. 4.26. Moffat residual of F2M2345-1003. Shown in (a) is the residual image obtained by subtracting the Moffat model from the original image and in (b) a 3D plot of (a). With the power law index of 0.948848, this residual is very similar to the Lorentzian result.

By eye inspection, we conclude that the best subtraction comes from the Moffat model. As F2M2345-1003 is a source yet undetected by the HST, we use the SDSS image to produce a contour plot. We overlay the contours on top of the original average slice, result of which is shown in Fig. 4.27. Figure 4.28 shows the contours combined with the Moffat residual. In Fig. 4.27 we observe a bright region in the upper right part of the image that may be identified as the excited gas or an integrated star-formation region in the host-galaxy. This bright region is even more prominent in Fig. 4.28. We observe a good match between our images and the contour plots.

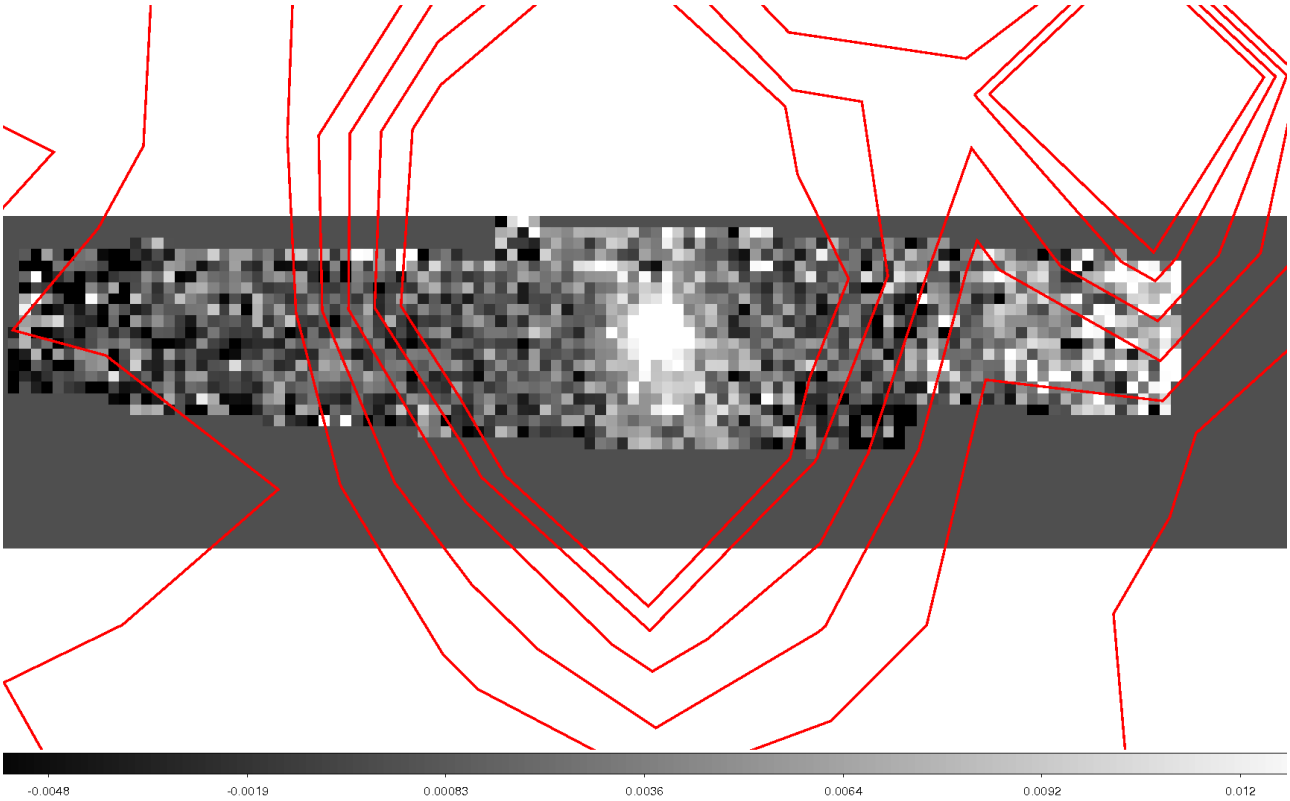

Fig. 4.27. F2M2345-1003 average slice with the corresponding SDSS contour plot shown in red. The brightest part of the galaxy is enclosed by the corresponding contour lines, demonstrating a good match. The upper right corner also fits well with the contour lines.

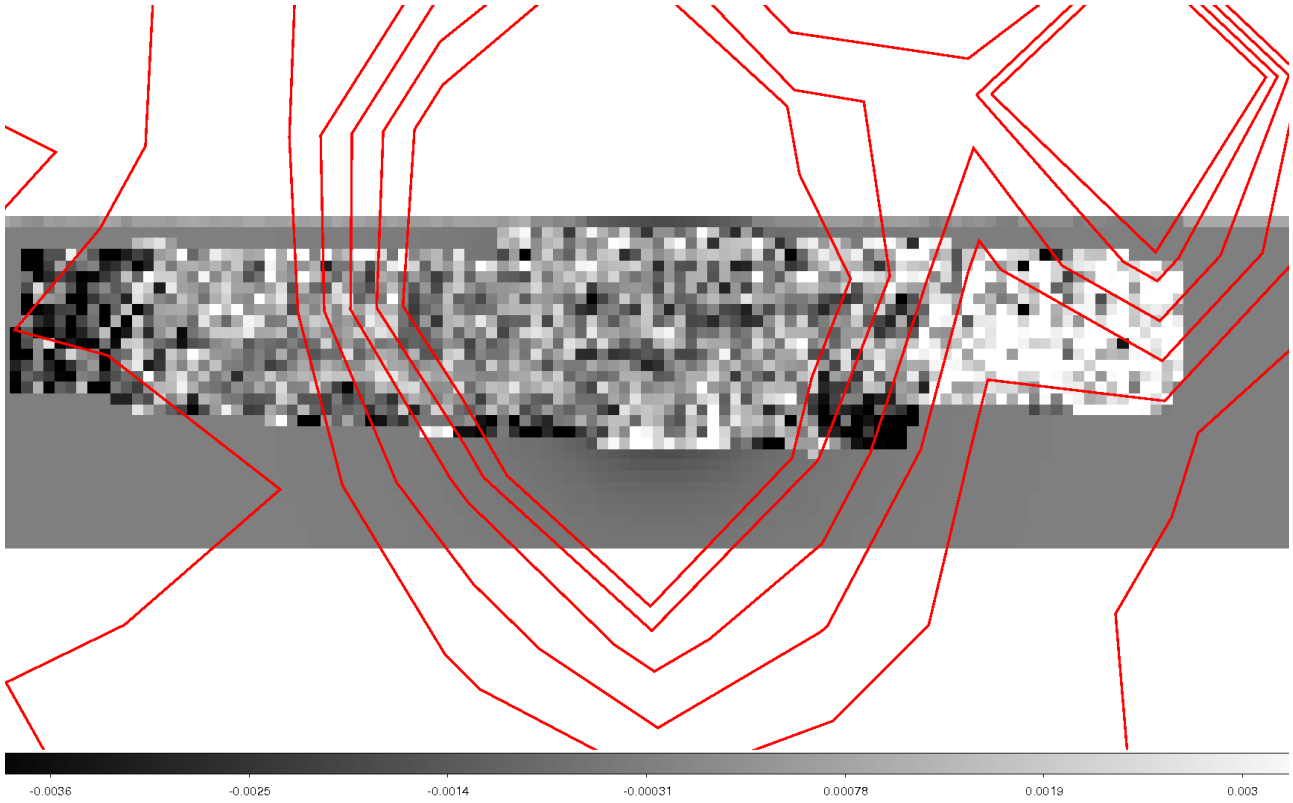

Fig. 4.28. F2M2345-1003 Moffat residual with the corresponding SDSS contour plot shown in red. Notice an increase in relative brightness of the upper right region as a consequence of quasar removal. The bright region matches the contours.

4.4 S82m2226-0032

4.5 S82m2226-0032

Source S82m2226-0032 is one of the faintest objects we observed during a relatively short 105-minute exposure time interval. After averaging the corresponding data cube over the wavelength space, from $N_\lambda = 0$ to $N_\lambda = 1476$, we observe a very low signal-to-noise ratio. In fact, as it can be seen in Fig. 4.29, the central nucleus' intensity is very close to that of its surrounding. This posed a challenge in terms of curve fitting, as the code would fit the entire bright extended area instead of the potential point source. To force the code to fit the central nucleus, we define the value of all the surrounding pixels to be 0, as shown in Fig. 4.30. Although this method squanders our data, it might still provide some insight into the structural details of the host

system.

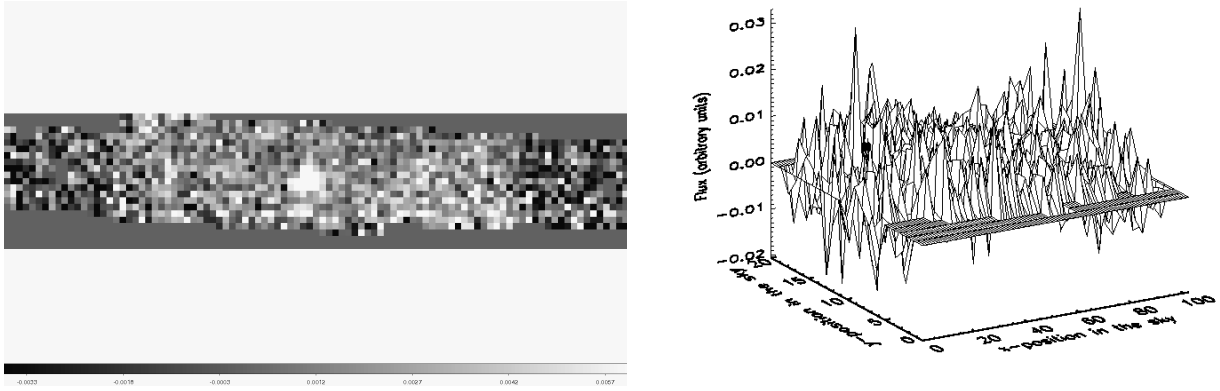

(a) Average slice of the reduced cube

(b) 3D plot of the average slice

Fig. 4.29. S82m2226-0032 averaged data cube. Shown in (a) is the object's position in the sky with the color gradient indicating the relative intensity at each pixel in arbitrary units. In (b) is shown a 3D plot of the slice in (a). No prominent peaks are observed in either (a) or (b).

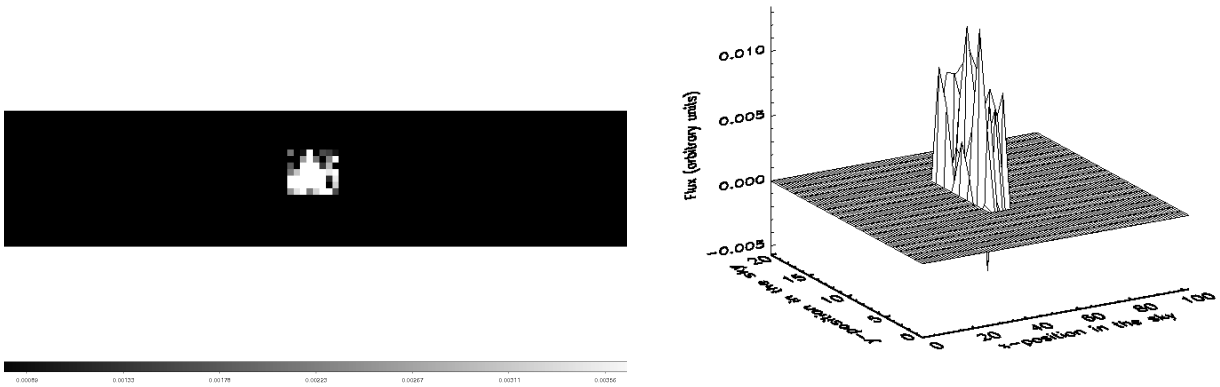

(a) Clipped average slice of the reduced cube

(b) 3D plot of the clipped average

Fig. 4.30. Clipped image of F2M2345-1003. Only the region of the central nucleus is remained with its original pixel values, while all the other pixels hold the 0-value, as can be seen from the average slice in (a) and the 3D plot in (b). This image is used for all the subsequent modeling procedures.

Analogously to the previously considered cases, we obtain parametric fittings to the clipped average slice. Figure 4.31 to Fig. 4.33 show Gaussian, Lorentzian, and Moffat fit curves.

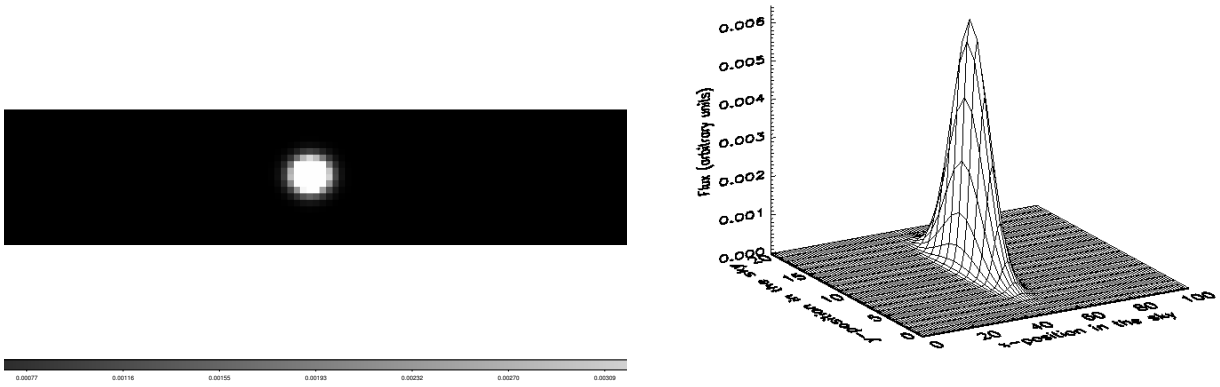

(a) Gaussian model of the clipped average slice

(b) 3D plot of the Gaussian model of the clipped average slice

Fig. 4.31. Gaussian model for the clipped S82m2226-0032. Shown in (a) is the Gaussian radial profile of the source, and in (b) a 3D plot of the found model in (a).

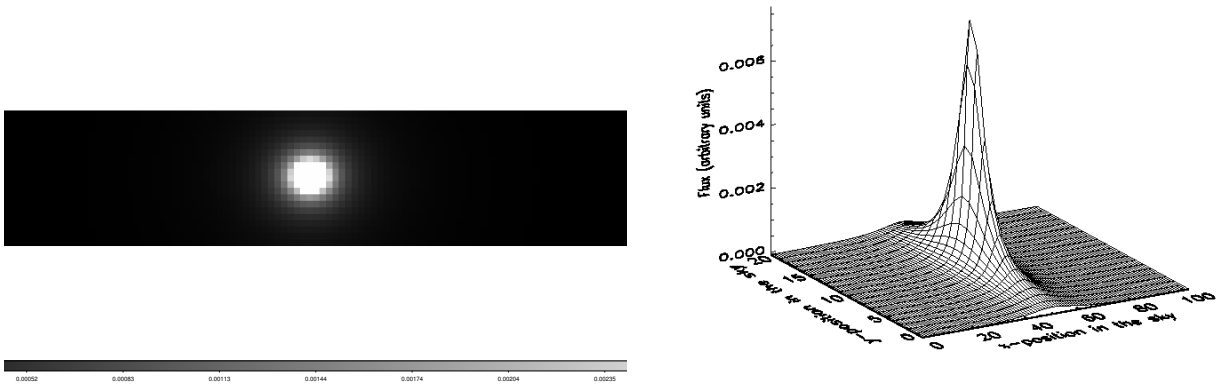

(a) Lorentzian model of the clipped average slice

(b) 3D plot of the Lorentzian model of the clipped average slice

Fig. 4.32. Lorentzian model for the clipped S82m2226-0032. Shown in (a) is the Lorentzian radial profile of the source, and in (b) a 3D plot of the found model in (a).

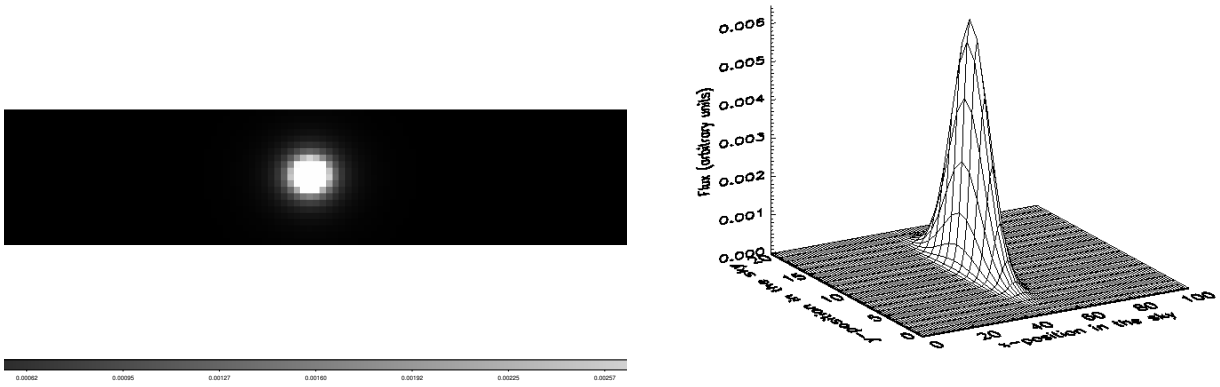

(a) Moffat model of the clipped average slice

(b) 3D plot of the Moffat model of the clipped average slice

Fig. 4.33. Moffat model for the clipped S82m2226-0032. Shown in (a) is the Moffat radial profile of the source, and in (b) a 3D plot of the found model in (a).

Following the previously established steps, we subtract the models from the original average data cube. Figure 4.34 to Fig. 4.36 show the obtained results.

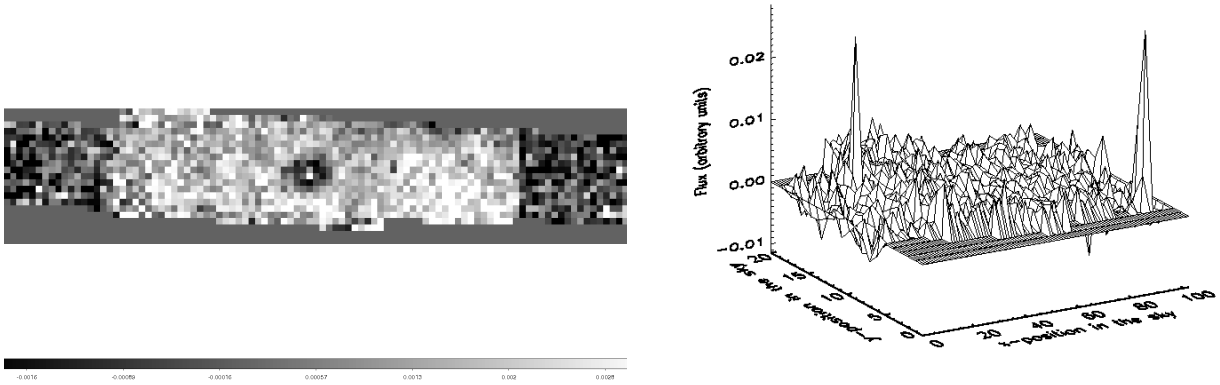

(a) Residual image after removing the Gaussian model from the original

(b) Gaussian residual, 3D plot

Fig. 4.34. Gaussian residual of S82m2226-0032. Shown in (a) is the residual image obtained by subtracting the Gaussian model from the original image and in (b) a 3D plot of (a). The central nucleus remains bright, surrounded by an over-subtracted halo. The bright region surrounding the dark doughnut is contains no information about the host-galaxy and is likely an artifact of the data reduction process.

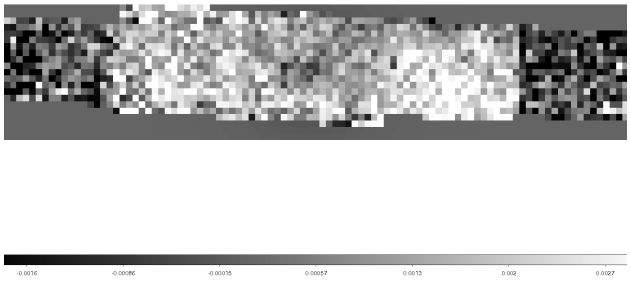

(a) Residual image after removing the Lorentzian model from the original

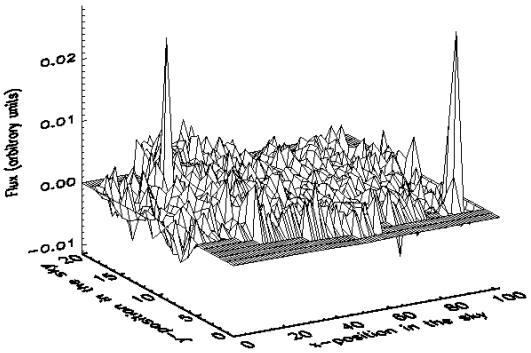

(b) Lorentzian residual, 3D plot

Fig. 4.35. Lorentzian residual of S82m2226-0032. Shown in (a) is the residual image obtained by subtracting the Lorentzian model from the original image and in (b) a 3D plot of (a). Similarly to the previous subtraction, no galaxy structure can be seen in this residual.

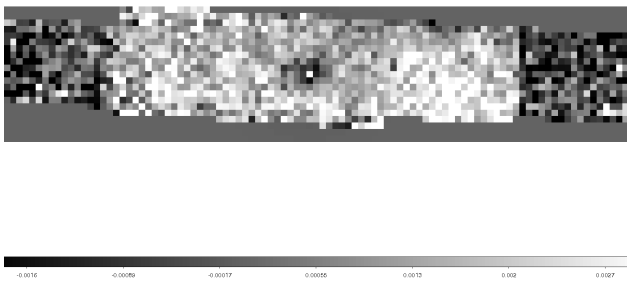

(a) Residual image after removing the Moffat model from the original

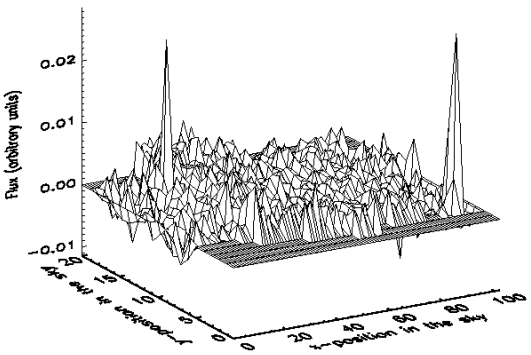

(b) Moffat residual, 3D plot

Fig. 4.36. Moffat residual of S82m2226-0032. Shown in (a) is the residual image obtained by subtracting the Moffat model from the original image and in (b) a 3D plot of (a). Again, no galaxy structure remains after the subtraction.

Due to a low signal-to-noise ratio, S82m2226-0032 proved to be a challenging target to analyze. After subtracting presumed models, no galaxy structure remained to be studied. In

order to address this issue, a longer total exposure time or/and a larger telescope is necessary to conduct this observation in depth. However, we still produce the SDSS contours to be overlaid over the original average image. Figure 4.37 demonstrates this result, with the bright region of the contour matching well the brightest region of the image, but with a slight offset in the south-east direction.

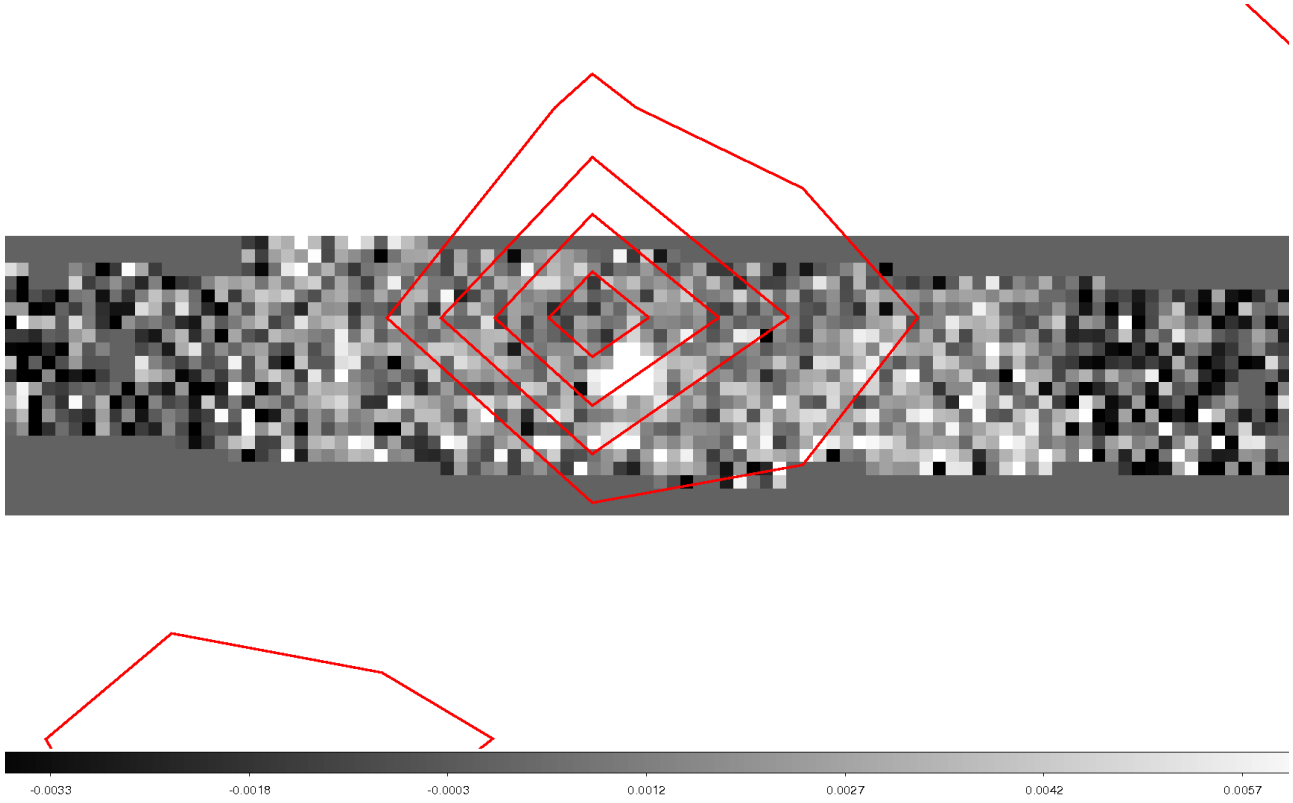

Fig. 4.37. S82m2226-0032 average slice with the corresponding SDSS contour plot shown in red. Contours match the position of the brightest region well, with a slight offset in the south-east direction.

5 Conclusion and Further Research

In this project, we successfully conducted the data reduction process using the OSIRIS pipeline in combination with the IDL code for six objects, out of which four contained analyzable data. We produced Gaussian, Lorentzian, and Moffat PSFs for each of these sources in order to eliminate any contamination coming from the central nucleus. Once quasar's contribution was removed, we considered the structural characteristics of the corresponding host-galaxies. Lorentzian and Moffat functions proved to be nearly-perfect models for F2M0825+4716, allowing for a study of bright regions surrounding the central nucleus. For F2M1656+3821, the best subtraction resulted from the Gaussian fit, with a small amount of quasar residuals. Despite the low signal-to-noise ratio that necessitated 2σ-clipping for F2M2345-1003, we were successful in producing a strong Moffat PSF for this source. Although prominent bright regions emerged when quasar's contribution was subtracted for all of the sources, suggesting a potential presence of excited gas or integrated emission from stars, further analysis is required to make a conclusive statement about star formation rates in considered galaxies. The first step to approaching a more quantitative analysis is flux calibration.

Furthermore, we extracted contour plots using the HST and SDSS data for our sources. Three out of four objects showed a slight shift in the south-east direction relative to their expected positions determined by their respective contour lines. A possible interpretation of this scenario is a recoil from a collision. However, considering the consistency in the general direction of the shift, it is more likely that it is a positional error in measurement encoded in the image headers from offsetting and tip-tilting. W.M. Observatory has been informed of the potential existence of this issue and it is currently being evaluated. Finally, one of the sources (S82m2226-0032) proved not to have high enough signal-to-noise ratio to provide any meaningful

interpretation of residual images. A deeper observation is necessary in order to improve these results.

A suggestion for an interesting consideration of our data would be utilizing the high spatial resolution of the OSIRIS instrument to produce spatially resolved velocity maps. Besides structural information, this analysis would provide a detailed insight into the kinematics of the each source, providing a powerful method into probing the stages of galaxy evolution.

Appendices

A Observing Logs

Table A.1. Observations conducted using the OSIRIS IFS in combination with the AO system. Listed are objects' names, their positions in the sky, redshifts z, K-magnitudes, filters used during observation, exposure times, total on-course exposure times, plate scales, and observation dates.

Object	R.A.	Dec	Redshift, z	K (mag)	Filter	Exposure time (s)	Total time (min)	Plate scale (arcsec)	Observation date
F2M0825+4716	08:25:02.04	+47:16:52.2	0.803	14.1	Kbb	600	210	0.1	Nov 5, Nov 6, 2012
F2M1507+3129	15:07:18.63	+31:29:39.8	0.988	15.1	Jn3	600	90	0.1	Apr 18, 2011
F2M1656+3812	16:56:47.10	+38:21:36.7	0.732	15.1	Kn4	600	80	0.05	Apr 18, 2011
F2M2345-1003	23:45:54.91	-10:03:29.1	0.263	14.2	Hbb	600	90	0.1	Nov 6, 2012
S82m2226-0032	22:26:06.22	-00:32:32.4	0.578	15.1	Kbb	900	105	0.1	Nov 5, 2012
UKFS0152+0020	01:52:43.18	+00:20:40.3	0.578	16.3	Zbb	900	60	0.1	Nov 5,2012

B Data Reduction

Data reduction of the obtained images was carried out using OSIRIS data reduction pipeline (DRP) routines in combination with Interactive Data Language (IDL) scripts. A detailed description of technical steps including scripts can be found in [2] and [7]. A brief discussion of the physical significance of conducting the reduction process is described in [1]. Below are reduction steps listed in the performed order as they were applied to F2M1656+3821.

B.1 Manipulation of dark frames

Dark frames are images taken with the closed shutter for a time interval equivalent to the iteration time for each object observed. All of the observations in this set were conducted with either a 600-s or a 900-s iteration time period. For each of these observations, a corresponding set of dark frames has been obtained. Dark frames are used to account for the time-dependent charge build-up, thermal noise, and can provide information about "hot" pixels or the potential cosmic ray collection. The final dark calibration frame is produced by combining and averaging multiple dark frames. This procedure is performed using the OSIRIS data reduction pipeline described in [2] and [7]. An example of the final dark calibration frame is shown in Fig.B.1. This frame is subtracted from all the subsequent images of the observed object.

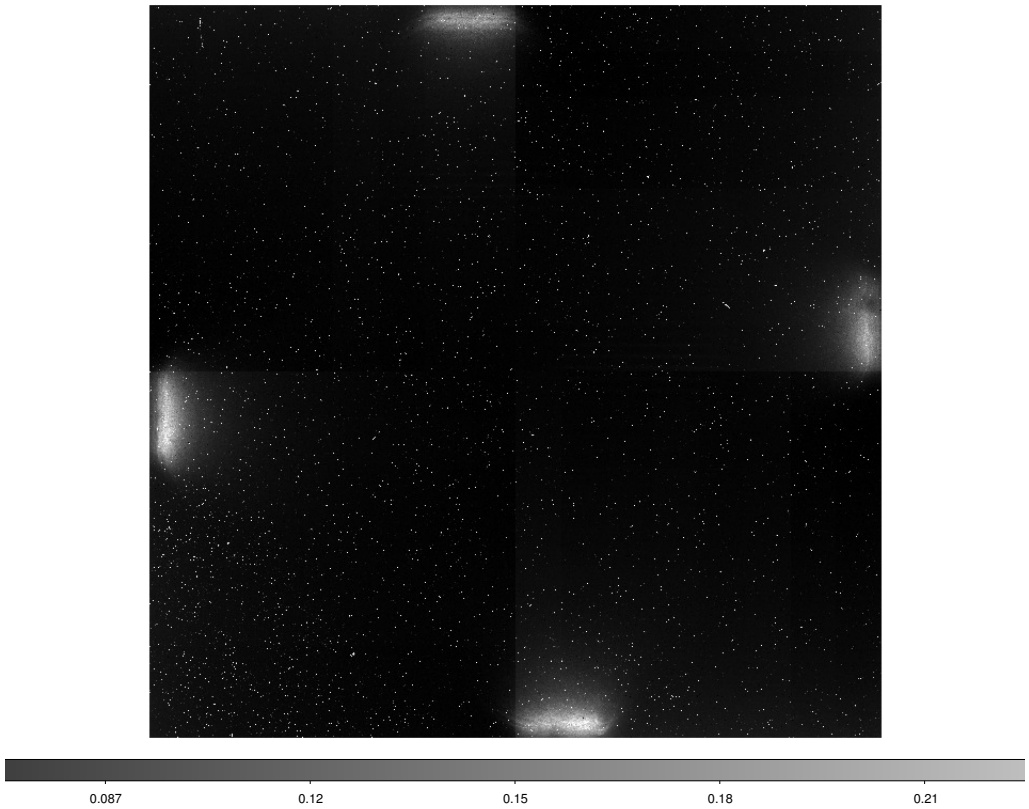

Fig. B.1. Final calibration dark frame for F2M1656+3821. Four 600-s dark frames were combined and averaged to produce the final frame. This frame is subtracted from all the subsequent images of F2M1656+3821.

B.2 Extracting the telluric (atmospheric) standard

Accounting for effects of the Earth's atmosphere is crucial to any infrared observation. To address this issue, we obtain images of a known close-by reference star (NGS), found under similar atmospheric conditions as our main target. Specifically, during the observation of F2M1656+3821, four star frames (HIP45382) were obtained. The first step to extracting the telluric standard for this observation consists of subtracting the combined dark frame produced in the previous step from each star image. Following this step, we extract spectra using calibration files from the OSIRIS data base found in [12]. After spectra are extracted, the data cube is assembled with a linear wavelength scale [7]. Figure B.2 shows a reduced frame for HIP45382.

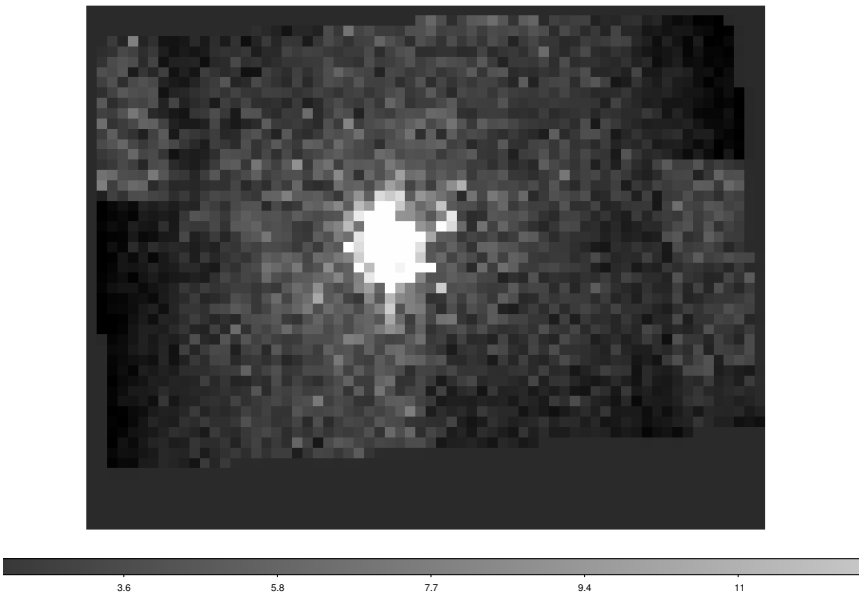

Fig. B.2. Reduced frame for F2M1656+3821's NGS, after subtracting the master dark frame and calibrating the wavelength.

Then, the four reduced star frames are combined into a single frame, using the `MEANCLIP` technique. The combined frame is shown in Fig. B.3. Following this step, a Gaussian curve is fit to the combined star image in order to find position coordinates of the peak, from where we extract the telluric spectrum shown in Fig. B.4. The code for this process can be found in [7].This spectrum is used as the telluric standard in all the subsequent steps of the data reduction of F2M1656+3821.

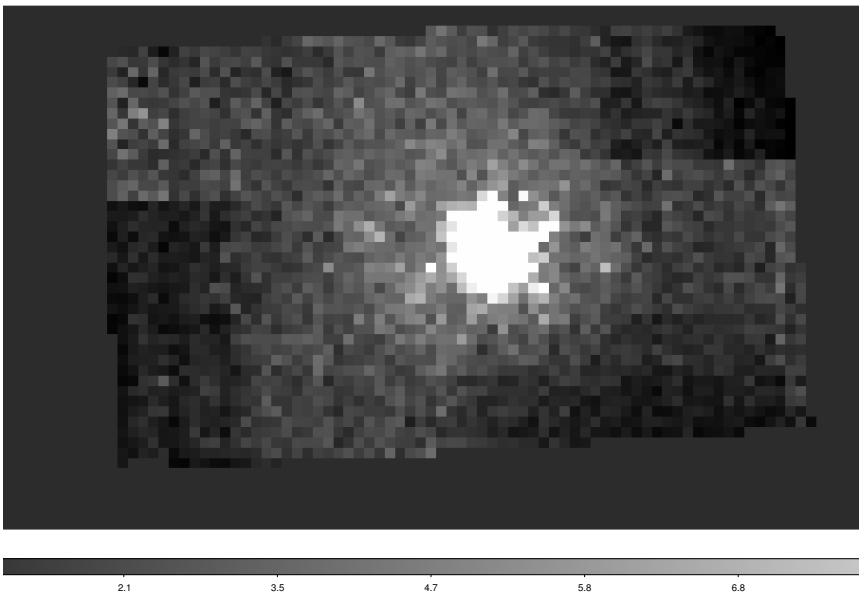

Fig. B.3. Reduced frame for F2M1656+3821's NGS, after subtracting the master dark frame and calibrating the wavelength.

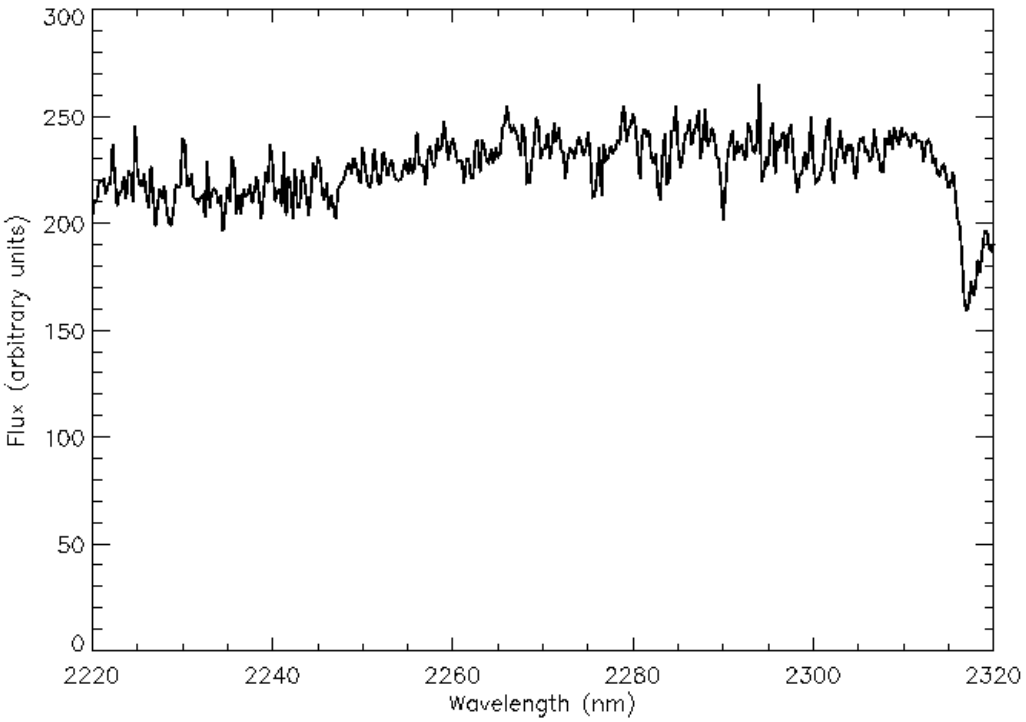

Fig. B.4. Telluric spectrum extracted from HIP45382. This spectrum is used as the telluric standard for the rest of the data reduction process.

B.3 Sky frames

To account for any emission lines from the bright infrared sky, we obtain two frames of an empty region of the sky close to our target, F2M1656+3821. These frames correspond to two different sets of observations of the main source. The third set, due to a time limitation on the telescope, only contains target images. For the third set, one of the previously taken sky frames was used as a model for the sky, as no large variations in the sky properties are to be expected within this time-frame. Reducing the sky frame is similar to the reduction of star frames previously discussed. The only difference is the consideration of the telluric spectrum. [7] and [2] contain step-by-step instructions and the code for this process. Shown in Fig. B.5 (a) is unreduced sky frame, and Fig. B.5(b) shows the sky frame after data reduction.

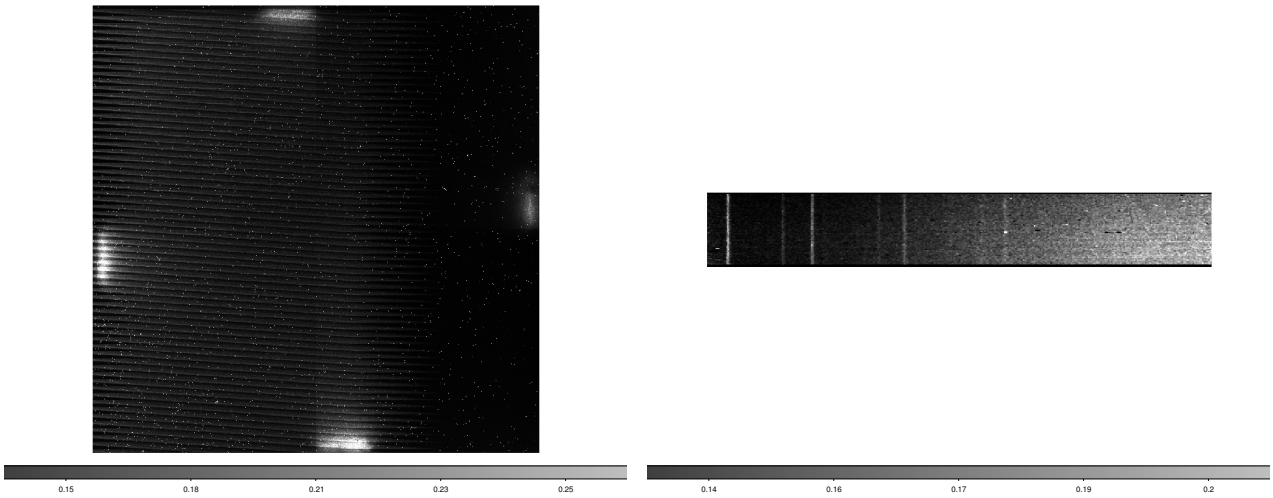

(a) Unreduced sky frame from the second set of observations of F2M1656+3821

(b) Reduced sky frame from the second set of observations of F2M1656+3821

Fig. B.5. Sky frames from the F2M1656+3821 observation (a) before the reduction process, and (b) after the reduction process. Notice the sky emission in (b), detected as bright vertical emission lines.

Once sky frames are reduced, they are subtracted from all frames of the science object. Once the the master dark frame, telluric standard, and reduced sky frames have been produced, we can proceed onto reducing the object frames.

B.4 Reducing and mosaicking the object frames

Reducing the object frames, simply put, consists of subtracting the dark and sky frame, and including the telluric corrections. Technical details of this process are described in detail in [7] and [2]. Once each object frame has been reduced, they are combined into a single data cube. This task consists of using one of the object frames as a reference image. from which offsets in every other frame are calculated. Once the offsets are found, all the individual frames are mosaicked together. Figure B.7(a) shows an unreduced frame of F2M1656+3821, and B.7(b) shows the final mosaicked image of the object. Image in B.7(b) is used for further analysis.

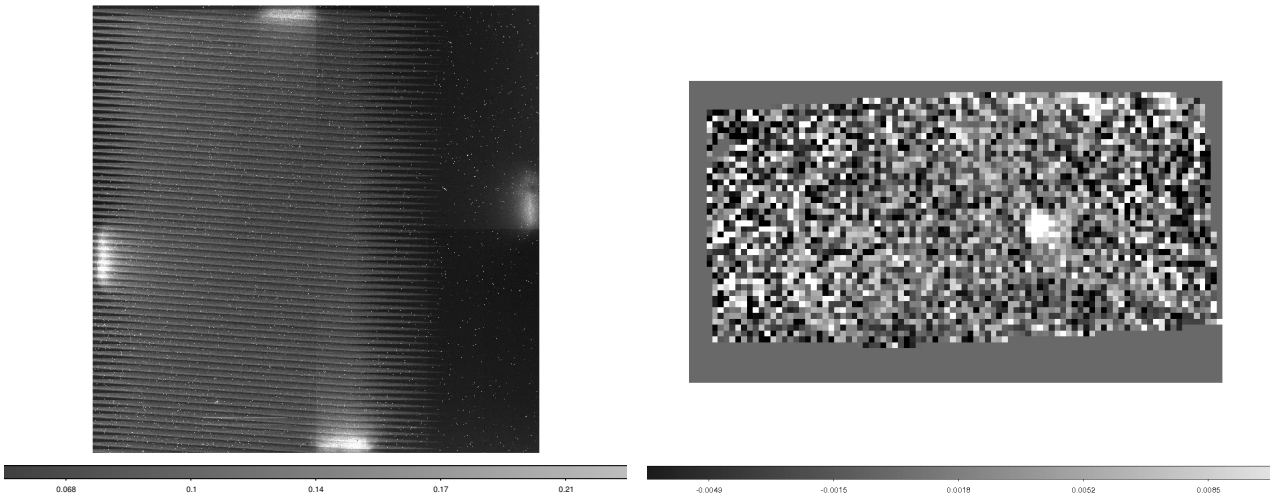

(a) Unreduced object frame from the second set of observations of F2M1656+3821

(b) Reduced and mosaicked frame for F2M1656+3821

Fig. B.6. Sky frames from the F2M1656+3821 observation (a) before the reduction process, and (b) after the reduction process. Notice the sky emission in (b), detected as bright vertical emission lines.

B.4.1 Data reduction of F2M1507+3129 and UKFS0152+0020

Data reduction of F2M1507+3129 and UKFS0152+0020 resulted in images with no central bright pixel region. These two sources, being the faintest within our observation set, require longer exposure times or larger telescopes in order to obtain meaningful images. Figure **??**(a) shows one of the reduced frames of F2M1507+3129, and (b) shows a reduced frame for UKFS0152+0020.

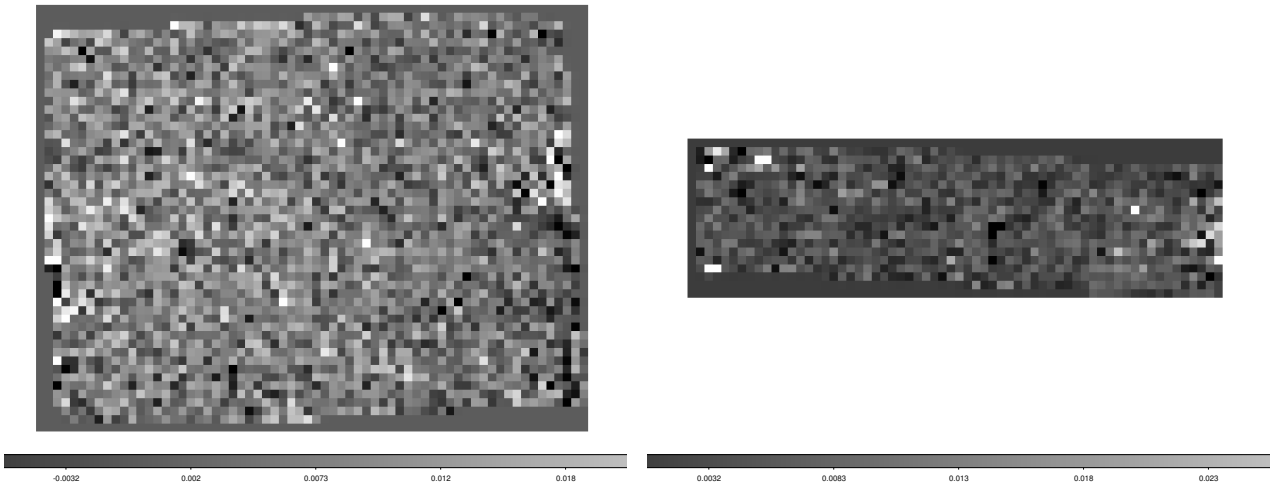

(a) Reduced object frame for F2M1507+3129

(b) Reduced object frame for UKFS0152+0020

Fig. B.7. Unsuccessful observation frames after the reduction process for (a) F2M1507+3129 and (b)F2M1507+3129. No strong light emission is detected in either frame, rendering the mosaicking procedure impossible with the tools provided in the OSIRIS pipeline.

C Additional notes on F2M1656+3821

Quasar F2M1656-1003 was observed on April 18, 2011. The filter used for this observation is Kn4, allowing a range of wavelengths from 2208 nm to 2320 nm. The Kn4 transmission curve is shown in Fig. C.1. Plate scale used for this observation was 0.05 arcsec alowing for a 2.1 $\times$ 3.2 arcsec^2 field of view, with 600-s integration time. A total of 80 minutes of target observation and 20 minutes of sky observation were conducted. A corresponding NGS was observed for 80 s, subsequently used to account for atmospheric effect. The final three-dimensional data cube of this object is shown in Fig. C.2.

We approximate the size of the galaxy to be $\theta = 0.4$ arcsec (8 pixels). Given the redshift $z = 0.732$ and current cosmological conditions, we find the angular size distance, D_A, to be 1518.5 Mpc [9]. Using this result, we report the observed linear size to be 2.9 kpc. Finally, we fit a Gaussian to examine the symmetry of the source, and report A FWHM of 2.3 pixels in the horizontal direction, and 2.2 pixels in the vertical direction. The small difference between these two numbers may be suggestive of a symmetric source.

Finally, we extract the emission spectrum of this source, over the region of the host-galaxy. We observe a prominent broad emission line, suggesting a relevant quasar activity. Figure C.3 shows the emission spectrum of F2M1656-1003. We identify a strong Pa$_\beta$ line (rest wavelength 1282.2 nm). Notice the potential splitting of this line, suggesting a possible dynamic system.

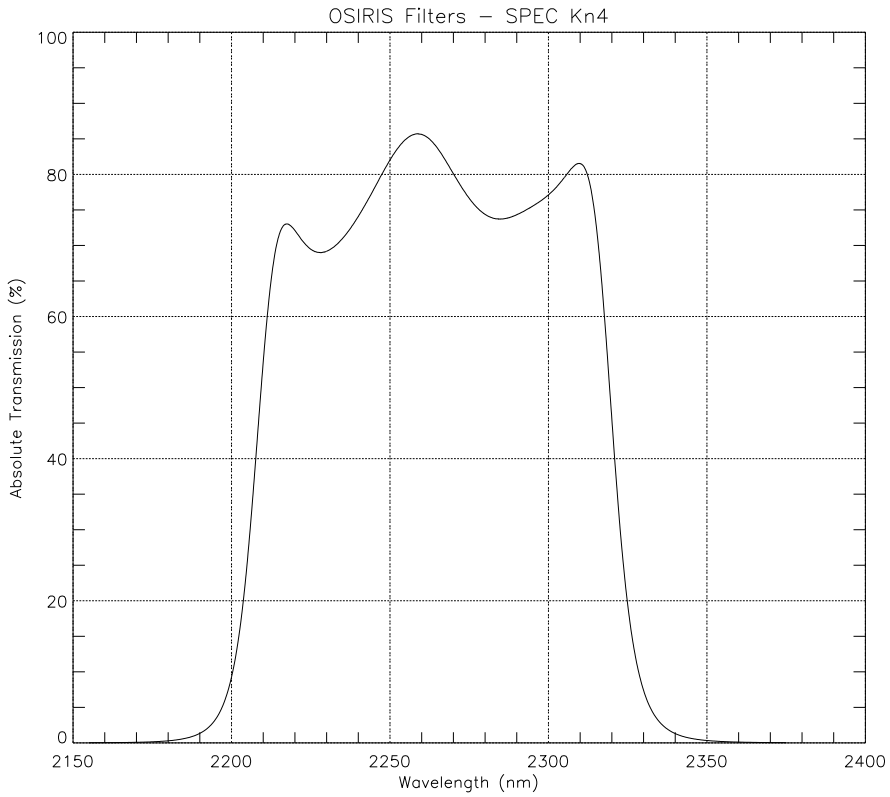

Fig. C.1. Transmission curve for the K-band Kn4 filter, used for the observation of F2M1656-1003, allowing for a transmission of 2208 to 2320-nm wavelengths.

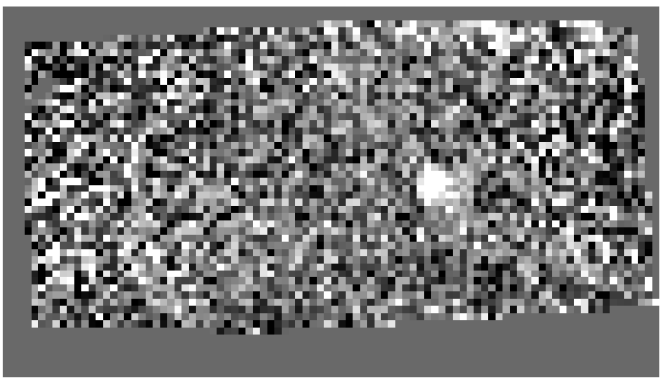

Fig. C.2. Reduced three-dimensional data cube for F2M1656-1003. Shown is the object's position in the sky. The color gradient indicates the intensity at each pixel in arbitrary units.

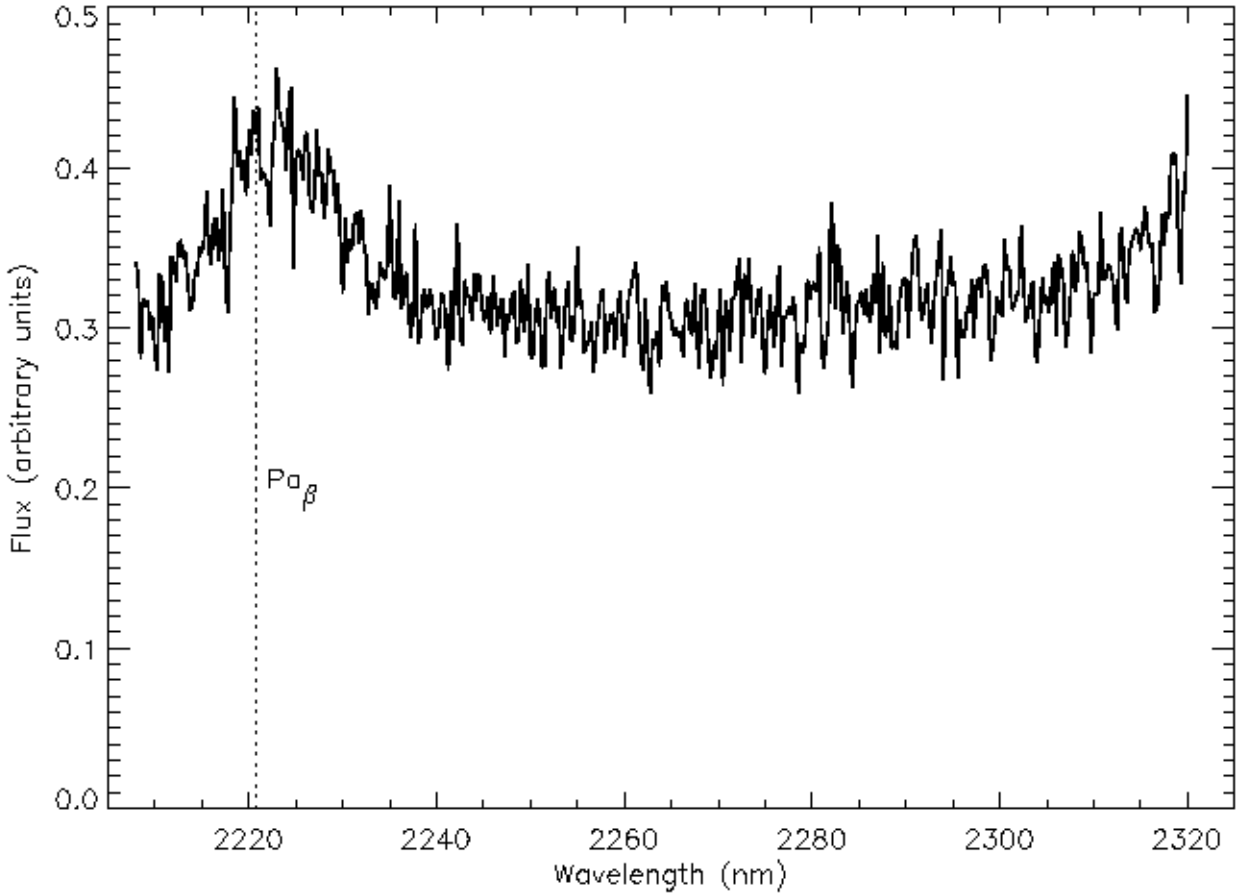

Fig. C.3. Emission spectrum of F2M1656-1003. Black vertical dotted line represents the redshifted wavelength of Pa$_\beta$ emission (rest wavelength 1282.2 nm). The redshift of the source is $z = 0.732$.

D PSF Determination Code Sample

To determine different models for the PSF, we produce IDL scripts shown below. Note that text following semicolon is reserved for comments (shown in blue). The following code was used to generate the Gaussian model and the Gaussian residual FITS images for F2M0825+4716:

```
pro loop_0825_slicesG,filename

cube=mrdfits(filename+'.fits',0,hdr)

;extension 0 is where the data is stored

nlam = 1665

;there are 1665 slices for the given cube

newcube=fltarr(nlam,111,22)

;creates an array to store the data in some of the next steps

Gausscube=fltarr(nlam,111,22)

for ii=5,nlam-6 do begin

slice=total(cube[ii-5:ii+5,*,*],1)/11.

;averages over ten slices

parinfo=replicate(fixed:0,limited:[0,0],limits:[0.D,0.D],7)

parinfo[4].limited=[1,1]

parinfo[4].limits=[56.,62.]

parinfo[5].limited=[1,1]

parinfo[5].limits=[8.,11.]
```

```
    ;sets limits on distribution parameters
    result=mpfit2dpeak(slice,a,parinfo=parinfo)
    ;creates a Gaussian and stores it under 'result'
    diff=slice-result
    ;creates the difference between the original slice and the model and stores
it under 'diff'
    newcube[ii,*,*]=diff
    Gausscube[ii,*,*]=result
    if total(result) lt 0 then print,ii
    ;notes pixels with negative fluxes
    endfor
    writefits, filename+'_modelG.fits',Gausscube,hdr
    writefits, filename+'_model_differenceG.fits', newcube,hdr
    ;writes FITS files of the model and the difference
    end
```

To call for the Lorentzian or Moffat distribution, use `result=mpfit2dpeak(slice,a,/lorentz)` for Lorentzian, and `result=mpfit2dpeak(slice,a,/moffat)` for Moffat function instead.

E σ-clipping Code Sample

A 2σ-clipping sample code that was used for F2M2345-1003 is shown below. Following a semi-colon are comments (shown in blue).

```
pro sigma_clip2sig, filename
cube=mrdfits(filename+'.fits',0,hdr)
;extension 0 is where the data is stored
nlam = 1651
;there are 1651 slices for the given cube
newcube=cube
for ww=5,nlam-7 do begin
m=mean(cube[ww,*,*])
sig=stddev(cube[ww,*,*])
for jj=0,13 do begin
newcube[ww,where(cube[ww,*,jj] gt m+2*sig),jj]=m
endfor
for kk=24,29 do begin
newcube[ww,where(cube[ww,*,kk] gt m+2*sig),kk]=m
endfor
for ll=0,53 do begin
newcube[ww,ll,where(cube[ww,ll,*] gt m+2*sig)]=m
```

```
    endfor
    for nn=69,118 do begin
    newcube[ww,nn,where(cube[ww,nn,*] gt m+2*sig)]=m
    endfor
    endfor
    ;only looking at pixels OUTSIDE the region of the central nucleus, substituting
their value with the mean if they exceed the threshold of 2σ deviation from the
mean
    writefits,filename+'_sigclip2sig.fits',newcube,hdr
    end
```

Bibliography

[1] M. Crnogorčević. The Co-Evolution of Post-Merger Galaxies and Dust-Reddened Quasars. *Senior Project report, Middlebury College*, December 2016.

[2] J. Larkin, M. Barczys, M. McElwain, M. Perrin, J. Weiss, and S. Wright. OSIRIS Users' Manual. *UCLA Infrared Laboratory*, 2010.

[3] E. Glikman, B. Simmons, M. Mailly, K. Schawinski, C. M. Urry, and M. Lacy. Major mergers host the most luminous red quasars at z $\sim$ 2: A Hubble Space Telescope WFC3/IR Study. *The Astrophysical Journal*, June 2015.

[4] P. F. Hopkins, L. Hernquist, T. J. Cox, and D. Keres. A cosmological framework for the co-evolution of quasars, supermassive black holes, and elliptical galaxies: I. galaxy mergers quasar activity. *The Astrophysical Journal*, June 2007.

[5] E. Glikman. Probing Quasar/Galaxy Co-Evolution: Integral Field Spectroscopy of Dust-Obscured Quasars. *Yale University Proposal*, March 2012.

[6] T. C. Urrutia. *Discovery and analysis of dust-reddened type I quasars – Finding the missing link in quasar evolution.* Thesis Dissertation. University of California, Davis, February 2008.

[7] M. Najarian. Using Integral-Field Spectroscopy of Dust Obscured Quasars to Probe Quasar/Galaxy Co-Evolution. *Senior Project report, Middlebury College*, May 2014.

[8] M. Schmidt. 3C 273 : A Star-Like Object with Large Red-Shift. , 197:1040, March 1963.

[9] N. Wright. *A Cosmology Calculator for the World Wide Web.* Available at http://www.astro.ucla.edu/wright/CosmoCalc.html (accessed May 2017). Department of Astronomy, UCLA.

[10] Marcos A. van Dam, David Le Mignant, and Bruce A. Macintosh. Performance of the Keck Observatory adaptive-optics system. *Appl. Opt.*, Oct 2004.

[11] B. Husemann. Integral Field Spectroscopy of Low-Redshift Quasars. *Thesis Dissertation. Universität Potsdam*, 2006.

[12] *OSIRIS Rectification Matrices*. Available at http://tkserver.keck.hawaii.edu/osiris/ (accessed May 2017).